

Project No. 14-7730

Experimental Determination and Modeling of Used Fuel Drying by Vacuum and Gas Circulation for Dry Cask Storage

Integrated Research Project

Travis Knight

University of South Carolina

Collaborators

University of Florida

South Carolina State University

John Orchard, Federal POC

Dennis Vinson, Technical POC

Final Report

Project: Experimental Determination and Modeling of Used Fuel Drying by Vacuum and Gas Circulation for Dry Cask Storage

Principal Investigator: Dr. Travis W. Knight, Professor and Director
Nuclear Engineering Program, University of South Carolina,
twknight@sc.edu, 803-777-1465

Co-PI: Tanvir Farouk, Jamil Khan, Elwyn Roberts, Joshua Tarbutton (UNCC), Jim Tulenko (UF)

Institution: University of South Carolina

Collaborators: Orano, Framatome, University of Florida, South Carolina State University

TPOC: Dennis Vinson

Federal Manager: J.C. de la Garza

Workscope: IRP FC-2

PICSNE Workpackage #: Project14-7730

Contract: DE-NE0008273, 10/01/2014 - 09/30/2018

Table of Contents

1. Abstract
2. Objectives
3. Milestones, Papers, and Presentations
4. Test Plan and Modifications
5. Experimental Design and Modifications
 - 5.1. Thermocouple Locations Deployed
 - 5.2. OES
 - 5.3. Ceria Pellets
 - 5.4. FHD Modifications and Operation
6. Summary of Results
 - 6.1. Freezing
 - 6.2. Drying Tests
 - 6.3. Range of Peak Test Rod Temperatures by Test Type
 - 6.4. Maximum Heater Rod and Chamber Thermocouple Temperatures by Test Type
7. Modeling

Acknowledgements

The investigators wish to thank the Department of Energy and the Nuclear Energy University Program (NEUP) for the support provided for this project. We also wish to acknowledge the essential contribution of our industry partners, Orano and Framatome, and specifically, Bill Bracey, Kevin Elliott, Tom Galioto, Jane He, and Arthur Niemoller.

1. Abstract

More than 120 drying tests were conducted using a mock fuel assembly with depleted uranium rods and heater rods to simulate decay heat. These tests followed standard industry practice for vacuum and forced helium drying (FHD). Both single effect tests evaluating a single fuel assembly or cask feature and combined effect tests were conducted. Single effect tests evaluated drying of a specific, known amount of water in a feature. Combined effect tests evaluated specific features and followed the flooding of the chamber, dewatering, and blowdown procedures before beginning the drying procedure. Specific simulated fuel assembly and canister features evaluated included PWR dashpot, BWR water rod, failed fuel rod, spacer disc, and Boral sheet. Ceria pellets were fabricated and used in the failed fuel rod to avoid issues of uranium contamination. A method of monitoring water content in the canister gas and gas stream was developed using optical emission spectroscopy (OES) in addition to monitoring of relative humidity in the chamber and in the vacuum lines.

2. Objectives

The spent fuel pool water from loading must be removed to avoid unnecessary corrosion and degradation of the fuel in storage and maintain the fuel in a retrievable geometry. Radiolysis of any retained water also offers the potential to create a flammable condition. The accepted drying process involves evacuation of the canister to less than 3 Torr and maintaining that pressure for 30 minutes after isolation from the pumping system. An alternate approach is to use helium (heated) circulated in the canister to achieve the same water vapor pressure. The goals of this effort was to utilize prototypical industry practice and equipment along with a full length mock fuel assembly to evaluate the drying process, quantify any water remaining, and develop models to predict the water remaining following a cask loading. This effort provides the scientific basis and validation of used fuel drying predictions needed by the industry and regulators.

Surfaces of fuel rods and other structures provide the opportunity for physisorbed and chemisorbed water that must be removed. The structure of the fuel assembly and cask are such that the possibility of trapped or retained water exists in places such as between rods and grid spacers. The dashpot on guide thimbles in PWR assemblies and BWR water rods can hold water up to some height dictated by weep holes. Flat surfaces within the canister such as spacer plates (discs) also provide locations where water may collect and be difficult to remove.

In addition to the surfaces of intact fuel rods, failed fuel rods may contain a significant amount of water that is difficult to remove. The plenum and any annular pellet spaces may be filled with water in addition to a significant amount of water may be chemisorbed and in the form of hydrates which will be difficult to remove. This effort examined simulated failed fuel rods in the drying process. There is concern that adiabatic cooling in the vacuum process could lead to the formation of ice crystals resulting in the retention of water in this way even though the cask may meet the prescribed criteria for dryness. Therefore, thermal imaging and thermocouples were used to investigate possible ice formation during drying.

3. Milestones, Papers, and Presentations

The following Milestones were accomplished for this project. Specific papers and presentations are also listed below.

Milestone Reports

- Test Plan, 6/30/2015
- Design of Experimental Facility, 6/30/2015
- Modeling Approaches, 9/30/2015
- Construction of Experimental Facility, 3/31/2016,
- Setup and Verification of Test System, 6/30/2016
- Performance of Drying Tests, 6/30/2018
- Development of Analytical Models, 9/30/2018

Papers

- Malik Tahiyat, Travis W. Knight, and Tanvir Farouk, "Plasma optical emission spectroscopy for water vapor quantification and detection during vacuum drying process," Review of Scientific Instruments, Vol.89, Issue 11, November 2018
- Shalloo, M., T. Knight, J. Khan, T. Farouk, J. Tulenko, "Vacuum Drying Experiments using a Mock Used Fuel Assembly", Waste Management Symposium (WM2018), Phoenix, AZ, March 18 – 22, 2018
- Tahiyat, M., Knight, T., Farouk, T., "Plasma Optical Emission Spectroscopy for Water Vapor Quantification in Used Fuel Drying Applications", Transactions Of the American Nuclear Society 2017 Winter Meeting, Washington, DC, Oct. 29-Nov. 2, 2017
- Shalloo, M., T. Knight, J. Khan, T. Farouk, J. Tulenko, "Vacuum Drying Experiments using a Mock Used Fuel Assembly", Transactions Of the American Nuclear Society 2017 Winter Meeting, Washington, DC, Oct. 29-Nov. 2, 2017
- Tahiyat, M., Knight, T., Farouk, T., "Plasma Optical Emission Spectroscopy for Water Vapor Quantification and Detection" International High-Level Radioactive Waste Management Conference, April 9 - 13, 2017, Charlotte, NC
- Knight, T. W., Jamil Khan, Tanvir Farouk, James Tulenko, " Experimental Determination of Used Fuel Vacuum Drying Using a Mock Fuel Assembly" International High-Level Radioactive Waste Management Conference, April 9 - 13, 2017, Charlotte, NC

Presentations

- "An Experimental Determination and Modeling of Used Fuel Drying by Vacuum and Gas Circulation for Dry Cask Storage", EPRI ESCP Workshop, Charlotte, NC, 8 November 2018
- "An Experimental Determination and Modeling of Used Fuel Drying by Vacuum and Gas Circulation for Dry Cask Storage", Spent Fuel, and Waste Science and Technology (SFWST) Annual Working Group Meeting, University of Las Vegas, Las Vegas, Nevada, United States Department of Energy, Office of Nuclear Energy, May 22-24, 2018
- "An Experimental Determination and Modeling of Used Fuel Drying by Vacuum and Gas Circulation for Dry Cask Storage", EPRI ESCP Workshop, Charlotte, NC, 14 November 2017
- "Vacuum Drying of Spent Nuclear Fuel for Dry Cask Storage", Savannah River Section, American Nuclear Society, Aiken, SC, 9 January 2017

- “An Experimental Determination and Modeling of Used Fuel Drying by Vacuum and Gas Circulation for Dry Cask Storage”, EPRI ESCP Workshop, Charlotte, NC, 30 November 2016
- “An Experimental Determination and Modeling of Used Fuel Drying by Vacuum and Gas Circulation for Dry Cask Storage”, EPRI ESCP Workshop, Charlotte, NC, 1 December 2015
- An Experimental Determination and Modeling of Used Fuel Drying by Vacuum and Gas Circulation for Dry Cask Storage, EPRI ESCP Workshop, Charlotte, NC, 4 December 2014

4. Test Plans and Modifications

The tests were executed according to the Test Plan which contained the procedures designed to reproduce as closely as possible the industry drying operations. The original Test Plan was submitted as a Milestone Report in July 2015. Forced helium drying (FHD) modifications and operations are described in Section 5.4.

Following dewatering and blowdown, vacuum drying tests followed a series of stages of evacuation from 760 torr or slightly greater depending on the pressure of backfill following blowdown. The individual stages with pressures and hold times are shown in Table 4.1.

TABLE: 4.1: Stages in Vacuum Drying with Hold Pressures and Times

Vacuum Step, Hold Pressure	Hold Time	Criteria to Proceed to Next Step
<50 torr	5 min.	<100 torr
<25 torr	5 min.	<50 torr
<15 torr	5 min.	<25 torr
<10 torr	5 min.	<15 torr
<5 torr	5 min.	<10 torr
<3 torr	5 min.	<5 torr
<2 torr	30 min.	<2.6 torr

In the course of carrying out these tests it was learned that some vendors and utilities were altering this procedure of following a number of stages in favor of a continuous evacuation to less than 3 torr. Therefore, a series of vacuum drying tests were conducted that began with evacuating the test chamber from ~800 torr (from backfill following blowdown) to <3 torr. This is followed by isolating the chamber and for 30 minutes then backfill test chamber with helium to between 500-900 torr. Next the chamber is re-evacuated to <3 torr and isolated from the pump to test for a 30-minute hold to confirm drying is complete. If it fails the criteria, the evacuation is repeated until the criteria is met. As with the standard procedure, the chamber is then opened to confirm removal of all water or quantify any remaining water.

The individual tests were conducted according to this Test Plan with revisions described below.

- Revision 1, 15 July 2016, updated schematics for dewatering, vacuum, and recirculation to represent the built system for setup and verification tests.
- Revision 2, 9 Jan 2017, updated failed rod procedures changing the approach to preparing the failed rod and conducting the test. This two-valve mechanism permitted the vacuum and fill of the failed rod to avoid trapped air in the rod.

- Revision 3, 3 May 2017, updated procedures for filling the chamber with deionized water considering the performance of the first Combined Effects tests. Revision 3 was made because it was important to make sure the chamber would be completely filled with water without damaging any equipment that was at the top of the chamber. A float switch was created to make sure the water level would be just below the equipment.
- Revision 4, 14 July 2017, updated procedures and schematics for dewatering, blowdown, recirculation, and vacuum mode. The procedures were updated following the installation of the forced circulation piping network and pump and to demonstrate how forced circulation will work during a test.
- Revision 5, 11 October 2017, changed procedure for forced circulation drying. Procedure was changed because of the inline heater and modifications made to the forced circulation line. Schematics were updated in revision 5 because it was decided to forgo the usage of a helium reservoir during forced circulation tests. Also, the cold trap was implemented into the schematic downstream of the desiccators to be used as a chiller for combined tests and forced circulation tests. The procedure for when to switch to the low mass flow meters for more accurate results during vacuum tests were added in revision 5 as well. The forced circulation part of the schematics was updated with new valve letterings. Also, the forced circulation was modified to ensure both the fill and vacuum lines were evacuated and backfilled correctly so that no air enters the system before and after the rod is inserted.
- Revision 6, 24 October 2017, updated schematics. Revision 6 was made because a pneumatic valve was added after the Swagelok valve that is connected to the helium tanks. This pneumatic valve was added to make it easier on the operator to start and stop helium flow. Also, the Hastings pressure gauge that was connected to the top of the chamber was moved to the fill line to get a more precise reading of the pressure in the fill line when it is being evacuated and backfilled.
- Revision 7, 14 December 2017, modified procedures for desiccator regeneration, quantifying water remaining in a test feature after test, and the outline. Changed the way desiccators were regenerated because it wasn't reaching maximum potential. During combined tests, desiccators were having to be cycled through frequently so the team created a procedure that incorporated helium flow and the cold trap during regeneration. The procedure for quantifying the water in the failed rod was changed. In quantifying the remaining water in the failed rod, a two-step process was implemented to see how much water can be dumped and how much water can be reinjected.
- Revision 8, 16 December 2017, updated procedures for outline and comments on filling failed test rod with water. Updated procedures changing the methods used to inject the failed rod and insert/remove the failed rod.
- Revision 9, 29 Dec 2017, updated schematic for forced circulation test and procedures for the in-line heater. The LabView script was modified in a way that the test operator can manual adjust the gain for the in-line heater which results in adjusting the in-line heater's temperature. This change would allow the in-line heater's temperature to be more stable during forced circulation tests. For revision 9, there was only one change made to the schematics with that being part of the fill line between valve Q and valve R was wrapped in heating tape and insulation tape. The heating tape was added to avoid heat loss during forced circulation tests from the exit of the in-line heater to the inlet of the chamber.

- Revision 10, 15 May 2018, modified forced circulation procedure, changed inline heater operation, post-test quantification, and Optical Emission Spectrometer (OES) collection. Revision 10 brought about a significant amount of changes for forced circulation tests. First off, the procedures for operating the in-line heaters was modified due to the LabView script being modified. This was done to make operating the in-line heaters a lot simpler by making it where the operator sets the initial current and the desired temperature for that respective in-line heater, then turns on the heaters. Prior to revision 10 the test operator would have to constantly be monitoring and changing the gain for the in-line heaters. Also, with the chamber now completely wrapped in heating tape to reduce heat loss. A procedure was added on how the heating tape would operate during all types of test. The procedure for taking OES samples during tests was revised. Lastly, the schematics were updated to show the installation of in-line heater 4 that is only used as a thermocouple at the exit of the siphon tube.
- Revision 11, 26 June 2018, includes updated schematics, added procedures for measuring rebound in relative humidity with the isolation of the chamber and piping network to provide an indication of dryness in Forced Helium Drying (FHD) tests, modified forced circulation procedures and OES data collection. Prior to revision 11, the heating tapes surrounding the external wall of the chamber were gradually increased in temperature throughout the test. The procedure was modified to set the heating tape to the desired temperature of 200 degrees Fahrenheit at the outset of the test. Also, revision 11 brought about the usage of rebound test during forced circulation drying. After the team was unable to clearly see when the chamber/rod is completely dry during a forced circulation test, a procedure was added monitor the amount of water remaining at the end of the test. By conducting the rebound tests, the operator can determine from the relative humidity sensors when the chamber reaches complete dryness. The backfilling pressure for the fill and vacuum lines was changed from 760Torr to 800Torr when prepping for a forced circulation test to ensure no air is leaking into the system. The OES procedures were slightly modified after seeing the settings that were mentioned in revision 10 wasn't showing the best results for all types of test. Lastly, the schematics were updated to show the OES line was moved to connecting directly to the chamber. This move was made after a vacuum test was conducted and seeing there was not a way to get readings during holds. This move also allowed the team to only get readings of what is inside the chamber instead of readings from inside the piping network.
- Revision 12, 7 August 2018, updated vacuum drying and thermal camera procedures. Prior to revision 12, before each vacuum test and ultimate pressure test would be conducted on the chamber. However, revision 12 brought a change where instead of conducting an ultimate pressure test, the operator would purge helium through the cooling gland penetration for 15 minutes. This change was made to speed up the process of prepping for a vacuum test. Originally the ultimate pressure test was to ensure the system started with only helium, however using this new procedure, OES readings still showed no signs of air inside the system. Also, revision 12 included how the team has been operating the thermal cameras during all types of tests.
- Revision 13, 6 September 2018, updated the vacuum drying procedures for both single effect and combined effect tests. An alternate vacuum drying procedure was tested similar to what some plants were using. Holds throughout the test were removed and instead, the chamber was evacuated to below 3 Torr where then a 30 minute hold was conducted. After the 30-minute

hold, the chamber is then backfilled to above 550 Torr but below 900 Torr. The evacuation process is then repeated until two successful below 3 Torr 30-minute holds are conducted. For a below 3 Torr hold to be successful, the pressure cannot increase over 2.9 Torr from starting pressure at the beginning of the hold.

Any changes to the test or deviations from the procedure are noted in the *Narrative* accompanying the report for that test.

5. Experimental Design and Modifications

The tests were conducted using the experimental facility described in the Experimental Design Milestone report submitted July 2015. In summary, a large vacuum chamber was designed in four segments to accommodate a full length BWR or PWR fuel assembly (see Figure 5.2). The upper segment has eight ports for instruments and vacuum or gas connections. There are six viewports along the length of the chamber on both sides to enable visual and thermal imaging. An Atrium 10A fuel assembly was modified by Framatome (then Areva) for use in experiments and used standard design fuel rods except that they contained depleted uranium. Twelve heater rods were located at the positions shown in Figure 5.1 and an interchangeable rod position was located at one corner. This interchangeable rod position permitted the simulation of a number of fuel assembly design features including:

- Simulated failed fuel rod (perforation at 175 cm in height and a Swagelok fitting at top for filling with a measured amount of water, CeO₂ pellets to simulate UO₂)
- PWR guide tube with dashpot (simulated by Zr-4 tube plugged at bottom, weep holes at 40 & 43 cm height)
- BWR water rod (Zr-4 tube, weep holes at 175 & 178 cm height plugged at bottom)

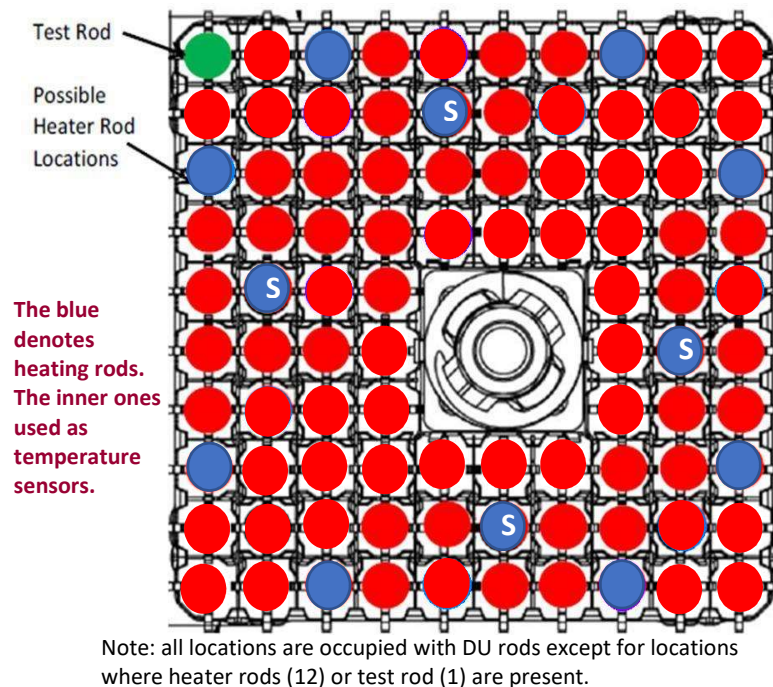
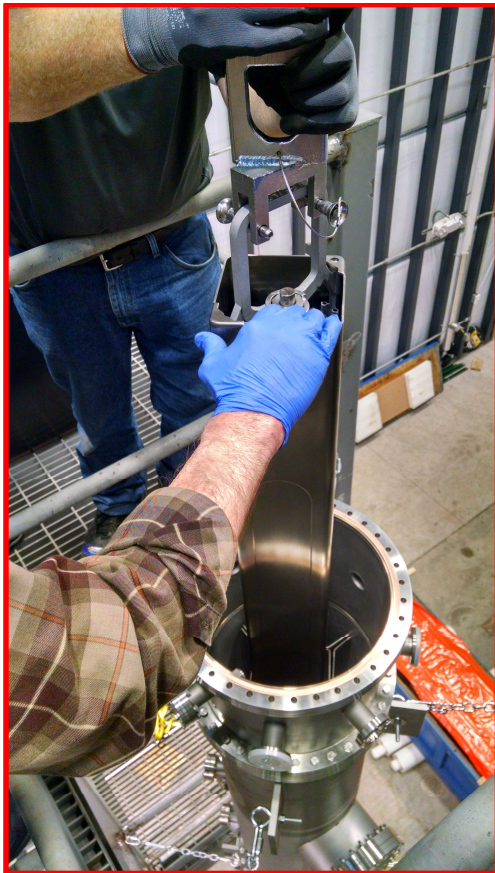
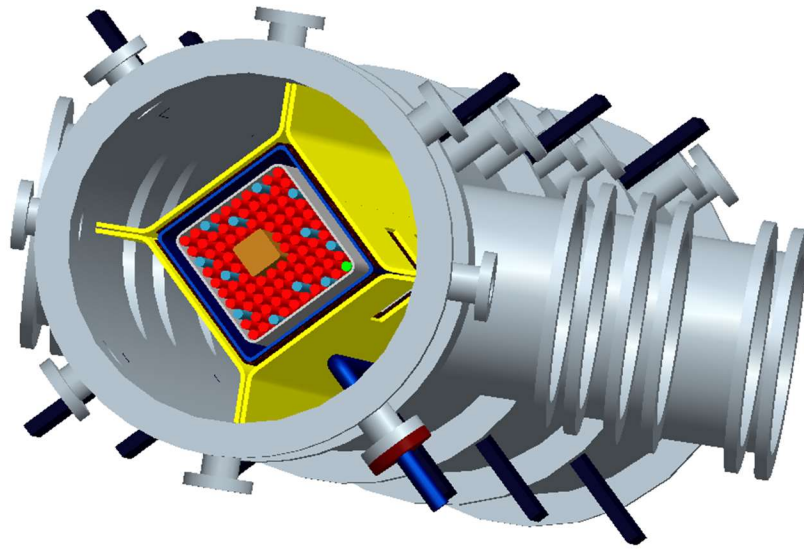
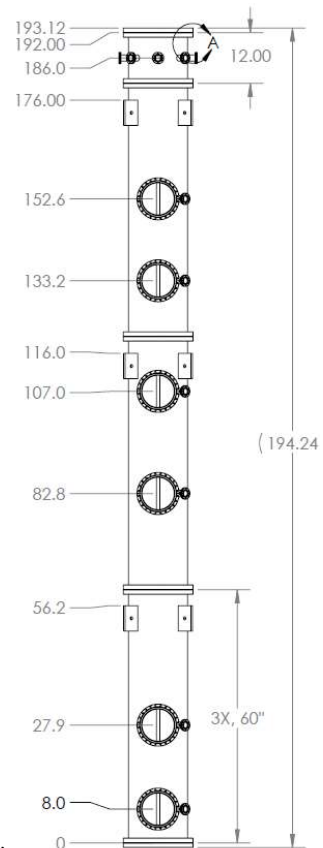


Figure 5.1: Illustration of the mock fuel assembly used in the experiments with the heater rods and an interchangeable rod position.



b)



c)

Figure 5.2: Vacuum chamber designed for use in drying experiments.

Throughout the performance of the tests changes were made to the experimental facility. These changes are described below to document and describe changes in the data collected and how it relates to the experimental features. The most evolved facility design is shown in Figures 5.3 and 5.4. More details on the design and operation of the components and systems for forced helium drying are given in Section 5.4.

- 8/8/16
 - Acoustic sensors attached to the outside surface of the vacuum chamber. This was to accommodate investigators from another NEUP-IRP and has no impact on the collection of UFD data.
- 10/19/16
 - Attached a manual valve between KF4 and KF5
- 10/20/16
 - The OES was re-connected to the piping network, because a leak rate test had been performed to test the sealing of the piping network without the OES connected.
- 5/5/17
 - Modified the spacer disc to now have a base and sit in the chamber at 25.9-degree angle, so the thermal camera could see the water inside the water tray.
- 5/10/17
 - Reconnected the thermal camera after adjusting settings affecting when the camera is out of range during testing.
- 5/16/17
 - The basket and rail thermocouples at viewport 2 were giving an erroneous reading and were found to be broken so a spot welder was used to fix the wires and reattached them to the basket and rail inside the chamber.
- 5/31/17
 - Removed viewport 1 thermocouple on the chamber bottom and attached to the siphon tube to detect freezing. This was done after seeing temperatures at viewport 1 decrease during combined vacuum tests.
- 6/8/17
 - Put heating tape on the line before the desiccator between V-K and V-B because of freezing in the pipe. During a combined vacuum test, freezing was noticed around the pipe between V-K and V-B using one the thermal cameras. The heating tape was added to avoid any ice form inside the lines.
- 6/9/17
 - Moved the thermocouple pressure gauge that was attached to the chamber that was not being used and put it upstream of the desiccator between V-B and the desiccators. This pressure was used to detect the pressure in the line before the desiccator. The reason this was done was to see the difference in pressure before and after the desiccator.
- 6/9/17
 - The back of the spacer disc was cut in order to see the test rod, heater rods, basket, and rail at viewport 2 while the spacer disc is inside the chamber.
- 7/5/17

- A grounding wire for one of the heater rods not well connected to the ground clamp. The grounding wire was reattached and all other screws were tightened to ensure they would not come unattached.
- 7/15/17
 - Added manual inline valve, M-K, to prevent intrusion of air during the transition from blowdown to vacuum drying. Before there was just a 3-way tee connection that would be disconnected and blanked off which would allow air to get inside the system. This valve now eliminates any possibility of air getting into the system at the end of blowdown.
- 8/22/17
 - Installed cold trap downstream of the desiccators to be used during combined vacuum tests. The intention was to capture moisture getting passed the desiccators. A manual valve was added before the cold trap and after M-F and M-H so that the cold trap could be isolated and removed from the system at any time.
- 9/27/17
 - Wrapped the external wall at the bottom of the chamber, between viewport 1 and viewport 2, with heating tape after seeing freezing occur during a combined vacuum test. The thought is that the freezing might create an ice plug which is preventing the system to dry. This heating tape compensates for the abnormally lower heat generation at the bottom of the chamber due to the power shape of the heater rods and the non-heated pedestal at the bottom.
- 10/11/17
 - In-line heater 1 installed and wired to PXI (One New Data File for inline heater power and temperature others).
- 10/18/17
 - New Optical Emission Spectrometer was installed. The team also switched to new OES software instead of using LabVIEW to get more accurate results during tests.
- 1/3/18
 - Detached vacuum line and V-A from vacuum pump on third level. Detached Digi-Vac (DV) pressure gauge from third level. This was done to conduct pressure tests on the new in-line heaters.
 - Attached in-line heater #2 between V-A and DV pressure gauge for leak rate testing
 - Attached in-line heater #3 between V-A and DV pressure gauge for leak rate testing
- 1/4/18
 - Switched the type of heating tape and wrapped exit of the siphon tube between V-K and V-B to prevent freezing during combined tests. The heating tape that was originally between V-K and V-B was moved to be between V-Q and V-R to avoid any heat loss from the in-line heaters and the chamber during forced circulation tests.
 - Installed in-line heaters #2 and #3 into the piping network.
- 1/5/18
 - Wired in-line heaters #2 and #3 to watt transducers and PXI (Two New Data Files for inline heater power and temperature others). This was done so the in-line heaters can be controlled and monitored from LabView.
- 3/15/18

- Wrapped heating tape around the entire chamber. This is to reduce heat loss particularly during forced circulation tests.
- 3/16/18
 - Installed power controllers for each heating tape. Each heating tape will be controlled and monitored through the power controller. There is a total of 10 power controllers for the entire chamber.
 - Attached 8 total thermocouples to the external wall of the chamber and the inlet and outlet of the chamber with their locations shown in Table 3. This was done particularly for the modeling team so they can accurately see what the heat load is surrounding the chamber.
- 3/19/18
 - Wrapped insulation around chamber, to reduce loss of heat from heating tape. The only part of the chamber that was not wrapped was the very top of the chamber and each viewport flange.
- 4/10/18
 - Installed new heating tape to replace old heating tape that had become faulty. This heating tape was located just below viewport 3. The heating tape went bad on 4/3/2018.
- 5/4/18
 - Replaced vacuum line between V-K and V-B with new lines including new in-line heater. In-line heater #4 is only to be used as a thermocouple. The goal is to find the temperature of the helium exiting the chamber during forced circulation tests.
 - From the exit of the chamber to V-B was rewrapped in insulation tape to reduce heat loss during tests.
- 5/30/18
 - Replaced leaking V-K (pneumatic) at the chamber exit with a new pneumatic valve. During a forced circulation test, with the chamber isolated, a rebound test was conducted and it was noticed that helium from the chamber was leaking into the vacuum line. After the test V-K was replaced. Once V-K was replaced, the line was rewrapped with insulation tape to ensure there is minimal heat loss exiting the chamber.
- 6/13/18
 - Moved the OES sample line to attach to the chamber instead of the vacuum lines. This was done after conducting a vacuum test and getting very little readings of helium and water. Allowing the OES to directly attach to the chamber gave the readings a better representation of what is inside the chamber during all types of tests.

Vacuum Mode

Date Proposed: 6/14/2018

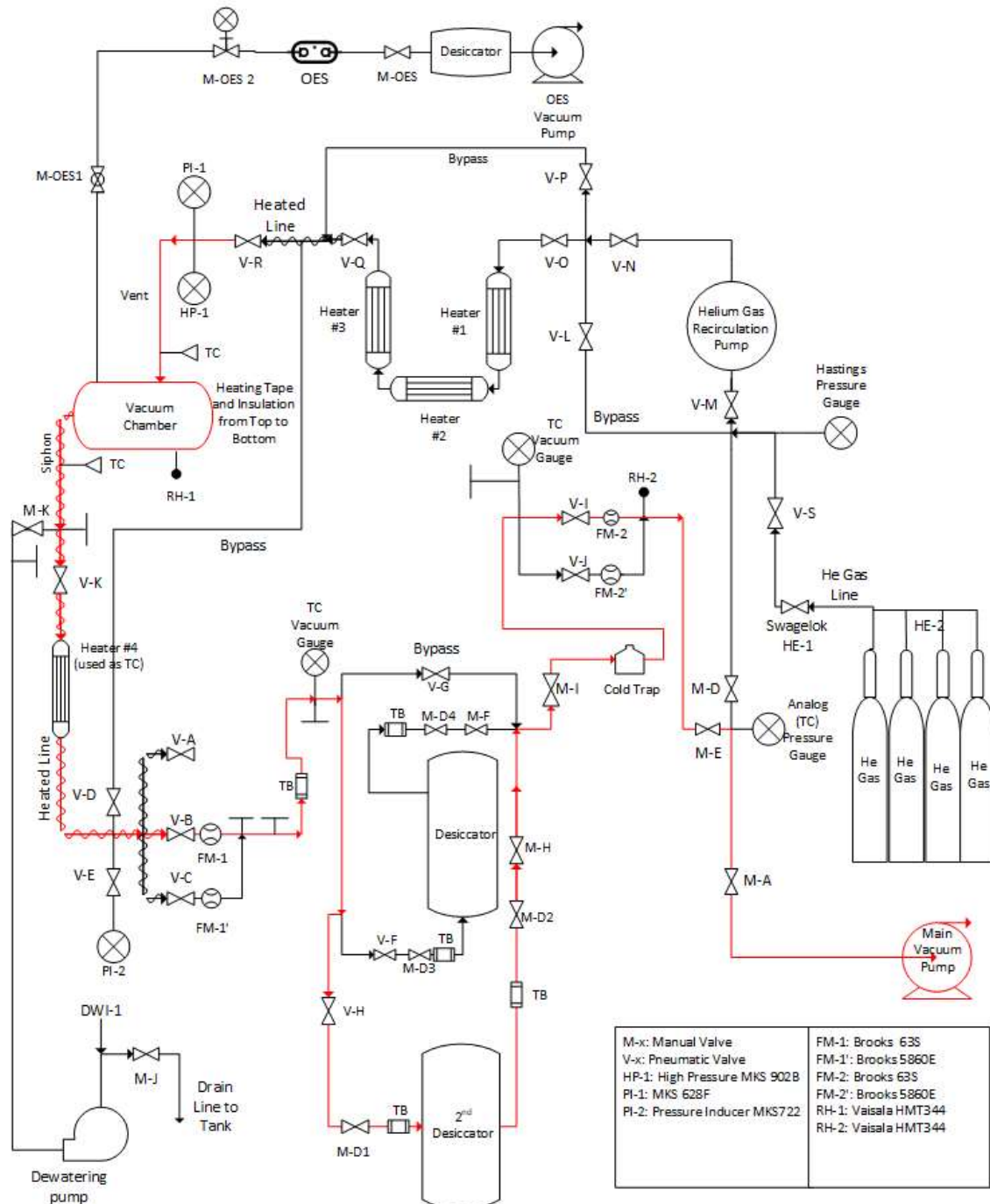


Figure 5.3: Schematic of the experimental facility design highlighting the operation of the vacuum drying tests.

Recirculation Mode

Date Proposed: 6/14/2018

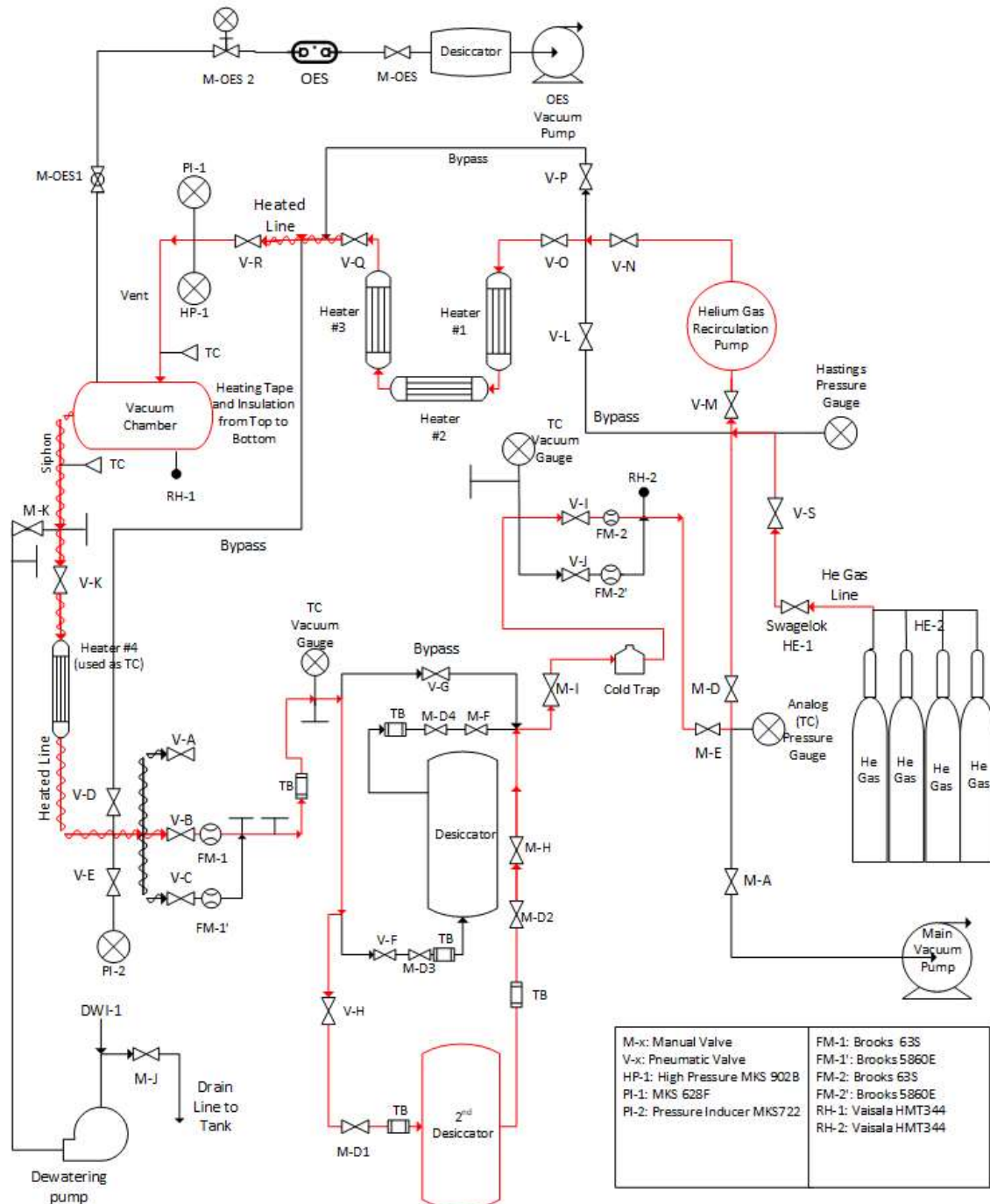


Figure 5.4: Schematic of the experimental facility design highlighting the operation of the FHD tests.

5.1 Thermocouple Locations Deployed

Temperature measurement in the chamber was important to ensure the testing achieved temperatures commensurate with industry operations and to provide data for validation models. Heater rods contained up to 8 type K thermocouples. Three type K thermocouples were also installed at each viewport location mostly on the channel, basket, and rails. Later, during the test phase, thermocouples were added to the outside of the chamber along with heating tape and insulation so that the chamber wall temperature could be controlled.

Heater Rods and Thermocouples

The heater rods contained thermocouples for measuring temperature internal to the fuel assembly. The locations of the heater rods are in the positions identified in Figure 5.5. In Table 5.1, each thermocouple is labeled with a different letter for each respective heater rod. Not all heater rods are the same type, which is why there are three types shown below in Table 1. For type 4 rods, there are no thermocouples attached.

Table 5.1: Location of thermocouples attached to each heater rod. The locations are the distance from the bottom of the chamber. Type 4 heater rods do not have thermocouples.

Letter	Color	type 1	type 2	type 3
H	Black	162.85	117.85	97.85
G	Red	151.85	109.85	87.85
F	Silver	137.85	97.85	77.85
E	Blue	129.85	93.85	68.85
D	Yellow	117.85	87.85	57.85
C	Green	109.85	77.85	48.85
B	Purple	97.85	73.85	32.85
A	Orange	87.85	68.85	12.85

*based on a heated length of 150inches, 12.35inches from heater rod threaded bottom to the bottom of the heated length and 0.5 inches from the heater rod threaded bottom to the bottom of the chamber.

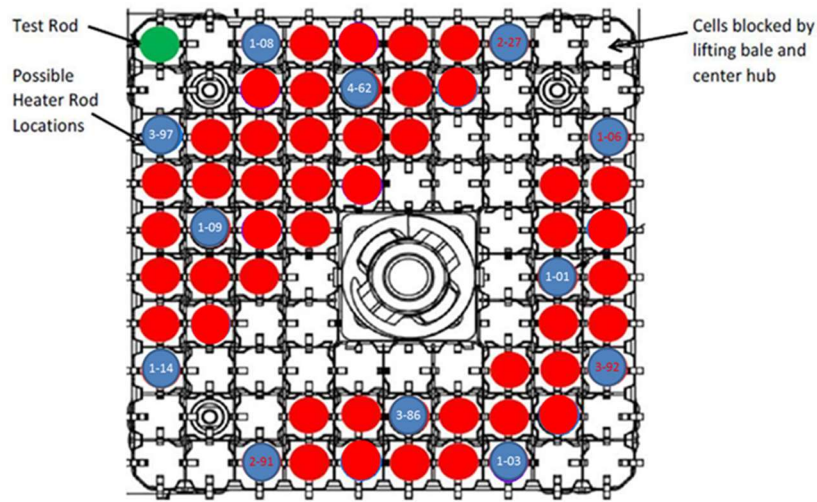


FIGURE 5.5: Illustration of the mock fuel assembly heater rod pattern. Heater rod number prefix indicates rod type and second part indicates specific rod. Blue indicates heater rod. Green indicates test rod position. All remaining rods are depleted uranium rods (red). Those depleted uranium rod positions not marked red are normally obstructed at the top by fuel assembly hardware.

Thermocouples at Viewport Locations

Figure 5.6 illustrates where the thermocouples are placed on the basket, rail, and channel. Specifics of thermocouple location is given in Table 5.2. Each thermocouple was spot welded on to the basket, rail, and channel at each viewport. As shown in the “UFD Data Template Timeline,” the viewport 1 channel thermocouple was moved to the siphon tube to identify freezing during each test.

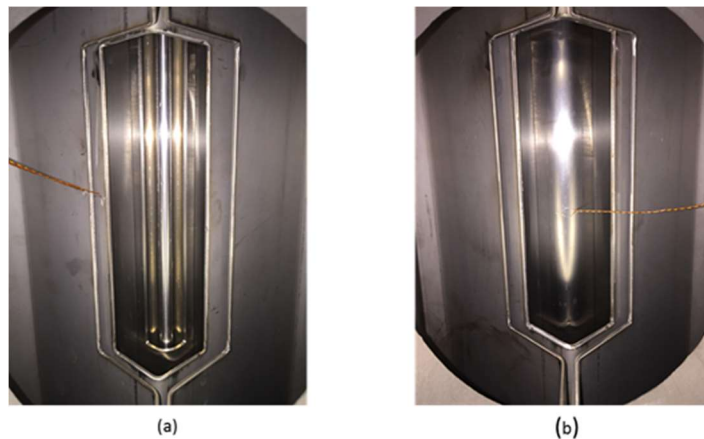


Figure 5.6: (a) shows how the basket and rail thermocouple look like at each viewport. (b) shows the channel thermocouple which is located on the opposite side of the chamber.

TABLE 5.2: The locations of additional thermocouples inside the chamber at different viewport locations as also shown in Figure 2.

Viewport	Location	Relative to chamber bottom (inch)
VP6	Basket	152.5
	Rail	152.5
	BWR channel	152
VP5	basket	132.1
	rail	132
	BWR channel	133
VP4	basket	106.4
	rail	106.5
	BWR channel	107
VP3	basket	83.2
	rail	83
	BWR channel	82.5
VP2	basket	27.5
	rail	27.5
	BWR channel	27.8
VP1	basket	8
	rail	8.1
	Bottom (moved to siphon tube after 5/31/17)	0
	Siphon tube (after 5/31/17)	5

Thermocouples External to the Chamber

Modifications were made to the chamber to install thermocouples, heating tape, and insulation on the outside of the chamber to control the chamber wall temperature. The locations of these thermocouples are given in Table 5.3.

Table 5.3: Location of the exterior chamber thermocouples that were added to system to analyze the temperatures on the chamber wall during each test

	Location	Relative to Chamber Bottom (inch)	Relative to the Test Rod Clockwise (degrees)
Attached to external chamber wall	VP1-VP2	18	270
	VP2-Flange	44	270
	Flange-VP3	73	270
	VP3-VP4	97	270
	VP5-VP6	145	270
	VP6-Top of Chamber	166	270
Attached to external piping network wall	Chamber Inlet	189	270
	Chamber Outlet	189	270

5.2 Optical Emission Spectroscopy

The methodology involves a direct current (DC) driven plasma discharge and optical emission spectroscopy for detecting as well as quantifying water vapor in a flowing gas stream under both trace and high-water vapor loading conditions. For the quantification of water content, the system was calibrated extensively.

The schematic of the plasma discharge cell setup for water detection together with the ancillaries that include the calibration unit and the diagnostics and measurement tools are presented in Figure 5.7. The plasma chamber consists of two solid cylindrical copper electrodes, each with a diameter of 9.525 mm. A thin 0.34 mm of insulation coating is provided on the outer periphery of the electrodes to prevent discharge initiation and formation on the cell wall and to further ensure that the discharge is confined within the inter-electrode gap, providing the perfect/optimum field of view for the optical probe to record the emission intensity. The inter-electrode separation is typically maintained at a spacing of 4 mm. The emission from the plasma discharge is acquired by an optical emission spectrometer (Ocean Optics HR 4000CG-UV-NIR) via an optical fiber (QP450-2-XSR) and the emission spectrum is observed and recorded using a spectroscopy software ('Oceanview' from Ocean Optics). The electrodes and the optical probe are housed inside a four-way cross tee having 69.85 mm flange diameter. The front flange is fitted with a fused silica glass window for visualization purpose. One of the electrodes is connected to a bellow arrangement (not shown here) to vary the inter-electrode separation if necessary. A varying inter-electrode separation distance provides the capability of initiating a plasma over a wide range of pressures by maintaining a constant pressure x distance (pd) value.

The pressure inside the plasma chamber is varied by means of a vacuum pump. For calibration of water vapor, the carrier gas mixed with water vapor was injected into the vacuum chamber as a result of the negative pressure differential created by the vacuum to eliminate the possibility of gas accumulation the piping network. Two calibrated mass flow controllers (MFCs) from MKS Instruments, each specified for different flow ranges, were employed for accurate varying of the gas mixture composition for the calibration of the emission spectrum. The respective operating ranges of the MFCs for helium gas are 0-200 standard cubic centimeters per minute (sccm) and 0-500 sccm. For both the MFCs, the control range is from 2 to 100% of full scale (F.S.) with an accuracy of $\pm 1\%$ of F.S. and repeatability of $\pm 0.2\%$ of F.S. measured with a digital pressure gauge (Teledyne Hastings 760s), with a Spellman power supply unit and a ballast of 10k Ω . The voltage across the plasma discharge and across the shunt is measured with a cathode ray oscilloscope (Agilent Technologies InfiniiVision MSO7054B) and a high voltage probe (North Star high voltage PVM-4). The emission from the plasma discharge is acquired by an optical emission spectrometer (Ocean Optics HR 4000CG-UV-NIR) via an optical fiber (QP450-2-XSR) and the emission spectrum is observed and recorded using a spectroscopy software ('Oceanview' from Ocean Optics).

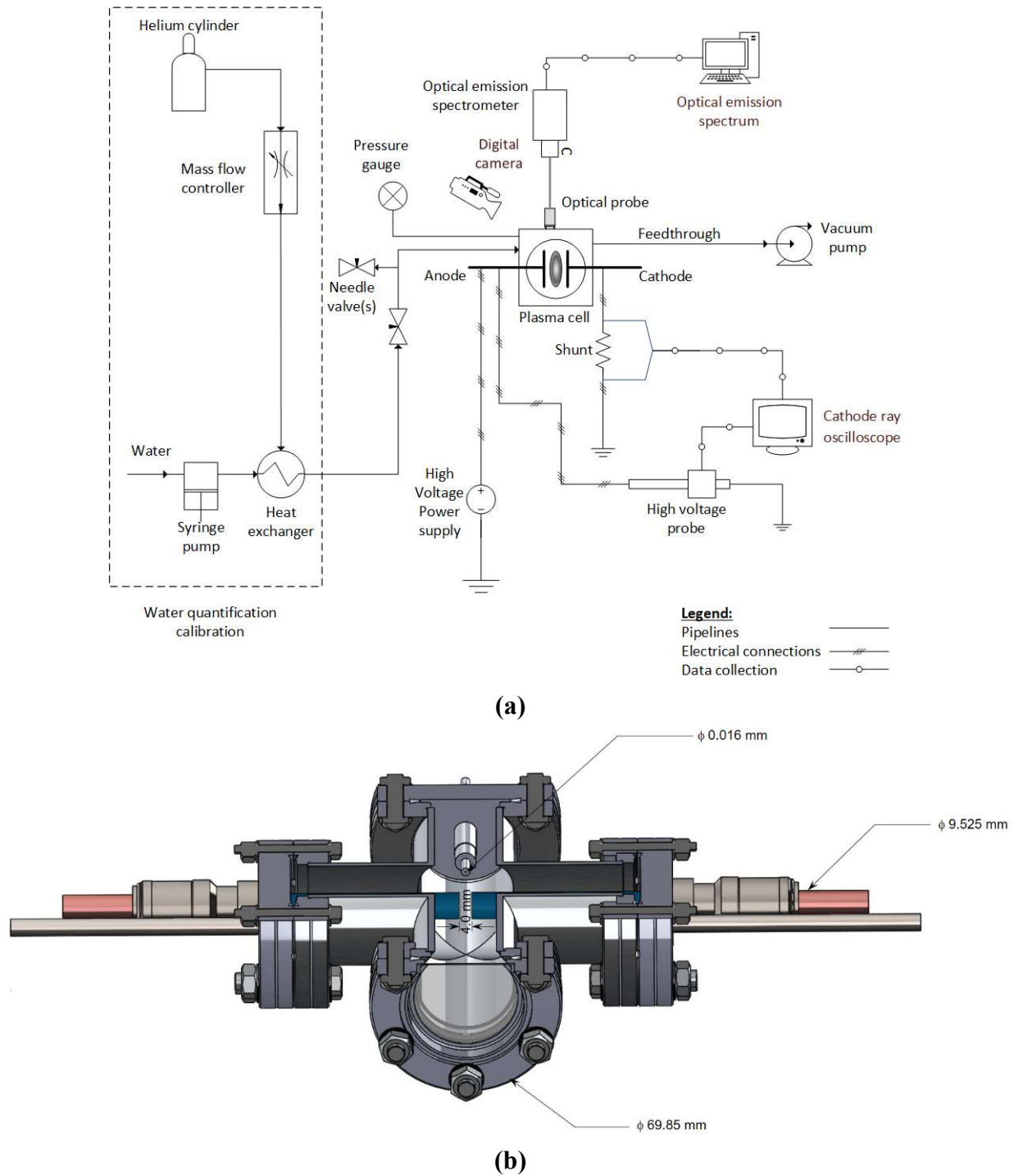


Figure 5.7. a) Schematic of the water detection system with the calibration equipment and associated diagnostics setup, b) sectional view of the plasma discharge cell.

For detecting water vapor concentration, the emission from H_{α} at 656.2 nm was employed. The H_{α} emission is the red visible spectral line generated by a hydrogen atom when an electron falls from the third lowest to second lowest energy level; this is the first transition in the Balmer series. The H_{α} is formed by the dissociation of water vapor to OH and H, which undergoes further electronic excitation

via electron impact reactions. The emission from H_{α} was chosen for detection purpose because of its very high sensitivity. Our experiments showed that even at a concentration of 2 ppm of water vapor, an emission from H_{α} was observed. The emission intensity of H_{α} was directly related to the water concentration level and thus was acquired for a range of water vapor concentration(s). In the calibration experiments, the water vapor concentration was systematically increased in the gas mixture by injecting a higher amount of water vapor into the helium stream.

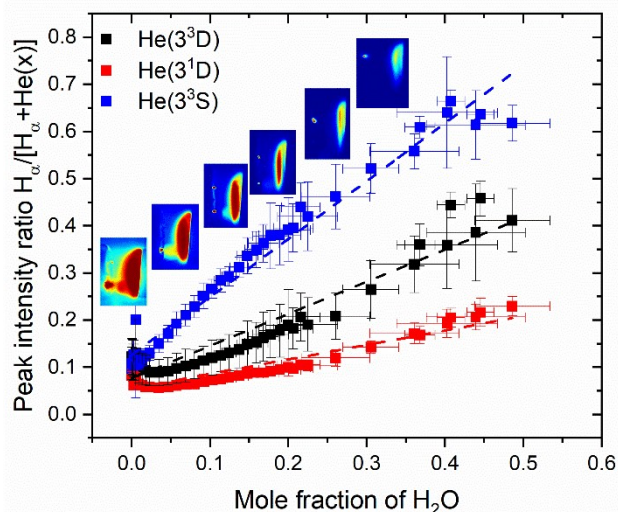


Figure 5.8. Peak normalized emission intensity of H_{α} as a function of water mole fraction at an operating pressure of 16.6 Torr and discharge current of 2.0 mA. The H_{α} emission intensity is normalized by $[H_{\alpha}+He(3^3D)]$, $[H_{\alpha}+He(3^1D)]$ and $[H_{\alpha}+He(3^3S)]$ separately.

Figure 5.8 shows the H_{α} intensity normalized by the summation of intensities of H_{α} and each of the three different He excited states [$He(3^3D)$ 587.6 nm, $He(3^1D)$ 667.8 nm and $He(3^3S)$ 706.5 nm] separately for a plasma discharge operating at 16.6 Torr pressure and having 2.0 mA discharge current. Four independent experiments were conducted and the error bars represent the standard deviation among the four experimental data set(s). For sensitivity purpose, the emissions from the three different excited states of helium were investigated. It can be seen that all three normalized H_{α} intensity signals increase linearly with increasing water vapor content. This suggests that the normalized H_{α} intensity can be used as a marker for water vapor detection and quantification. Despite the linear trend in all three of the emission intensity signals, it is apparent that as the water to helium flow ratio is increased beyond 0.5 the uncertainty in the measurements increases. This can be explained as follows: the plasma cell was operated at room temperature, which had been approximately at 290 K; along the vapor-liquid interface line in the phase diagram of water, 290 K corresponds to 15 Torr, which is lower than the operating pressure pertaining to Figure 5.8; thus, it is reasonable to assume that at higher partial pressure of water vapor, water may condense inside the plasma cell, resulting in nonlinearity in measurements. Exemplar false-colored images of the plasma discharge are also presented in Figure 5.8 as insets. It is apparent that with an increase in the water vapor content, the discharge radially constricts and at the same time its emission intensity decreases. The lower diffusivity of water vapor is primarily responsible for the observed overall radial constriction and hence the reduction in intensity. However, the emission

intensity of H_α decreases at a lesser gradient than that of excited states of helium. Therefore, despite the overall intensity decreasing, the fractional intensity ratio of H_α to that of $[H_\alpha + He(x)]$ has a positive slope. The radial constriction of the discharge also increases the current density for the same discharge current. It is observed that for a constant discharge current in the system the discharge constricted almost by a factor of ~ 4.0 for the entire range of moisture loading.

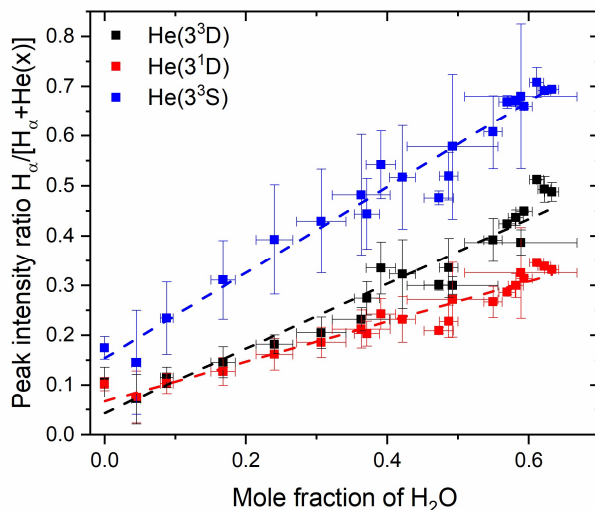


Figure 5.9. Peak normalized emission intensity of H_α as a function of water mole fraction at an operating pressure of 2.0 Torr and discharge current of 2.0 mA. The H_α emission intensity is normalized by $[H_\alpha + He(3^3D)]$, $[H_\alpha + He(3^1D)]$ and $[H_\alpha + He(3^3S)]$ separately.

To increase the maximum limit of water loading without possible condensation taking place, additional experiments were conducted at even lower pressure. These experiments were conducted at 2.0 Torr but for the same discharge current of 2.0 mA. Figure 5.9 summarizes the normalized H_α emission intensity for different water vapor fraction for those experiments. Similar to the 16.6 Torr experiments, four separate sets of experiments were conducted and the error bars represent the standard deviation. At 2 Torr, the emissions from the helium excited states are slightly different but a strong linear correlation is maintained nonetheless. At higher water loading the emission intensity of $He(3^3S)$ at 706.5 nm was found to reduce significantly but the $He(3^1D)$ and $He(3^3D)$ emission remain responsive over entire water vapor range of interest. This may be attributed to the wavelengths of these signals pertaining to similar electron transitional state ($1s.2p - 1s.3d$). The emission of $He(3^3S)$ at 706.5 nm is related to a smaller electron transition ($1s.2p - 1s.3s$) therefore as the helium concentration reduces in the gas mixture, the $He(3^3S)$ intensity decreases significantly faster resulting in a larger slope of $H_\alpha/[H_\alpha + He(3^3S)]$ as a function of the water concentration in the system. The error bars associated with $H_\alpha/[H_\alpha + He(3^3S)]$ are also significantly larger than the other two signals, which is strictly due to the larger variation in $He(3^3S)$ emission. Therefore, $H_\alpha/[H_\alpha + He(3^1D)]$ and $H_\alpha/[H_\alpha + He(3^3D)]$ signals are the ones deemed more reliable as water detection markers. It should be noted that at the low range of water mole fraction i.e. 0 – 0.05, a slight nonlinearity in the emission intensity is observed at both 2 and 16.6 Torr (Figures 5.8 and 5.9). This nonlinearity was observed consistently. A definitive understanding of the cause of this non-linearity is still being pursued at this stage.

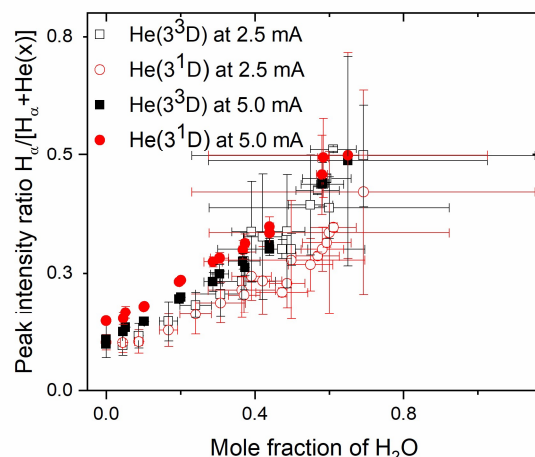


Figure 5.10. Peak normalized emission intensity of H_{α} as a function of water mole fraction at an operating pressure of 2.0 Torr for two different discharge currents of 2.0 mA and 5.0 mA.

To determine if the detection markers are insensitive to discharge current conditions, a range of experiments were conducted for different discharge currents at the same operating pressures. It was found that the normalized intensity signals of $H_{\alpha}/[H_{\alpha}+He(3^3D)]$ at different discharge currents collapsed on top of each other (Figure 5.10) and still maintains a linear trend. Since the plasma discharge that is used as the source for the different excited states is operated in the “normal glow” mode, an increase in the current does not increase the current density but the discharge size only – an increase in the discharge cross-sectional area. In the “normal glow” regime of operation, the discharge maintains a constant electron, ions and excited states number density value¹². A larger cross-sectional area/volume of the discharge results in a higher spatially averaged emission intensity acquired by the optical probe but the relative increase in the intensity of H_{α} with respect to that of each of $He(3^3D)$, $He(3^1D)$ and $He(3^3S)$ is similar. As a consequence, the normalized intensity remains insensitive to the discharge current. We would emphasize that this holds true for the “normal glow” regime of operation only.

Implementation in UFD System

The OES was connected to the vacuum piping network initially and later directly to the chamber (Figures 5.1 and 5.2). Samples were taken periodically (about every 15 minutes) during the performance of drying tests. Figure 5.11 is an example of a test showing an overall downward trend in hydrogen (water) content with drying. Because of the sensitive nature of the technique, water vapor deposited in the vacuum lines can provide a false indication of how much moisture is in the actual chamber. Therefore, it was decided to move the sampling point to attach directly to the chamber. Here it proved useful as an indicator of remaining water content in the chamber. Relative humidity was also a key measure especially during FHD tests (see Section 5.4).

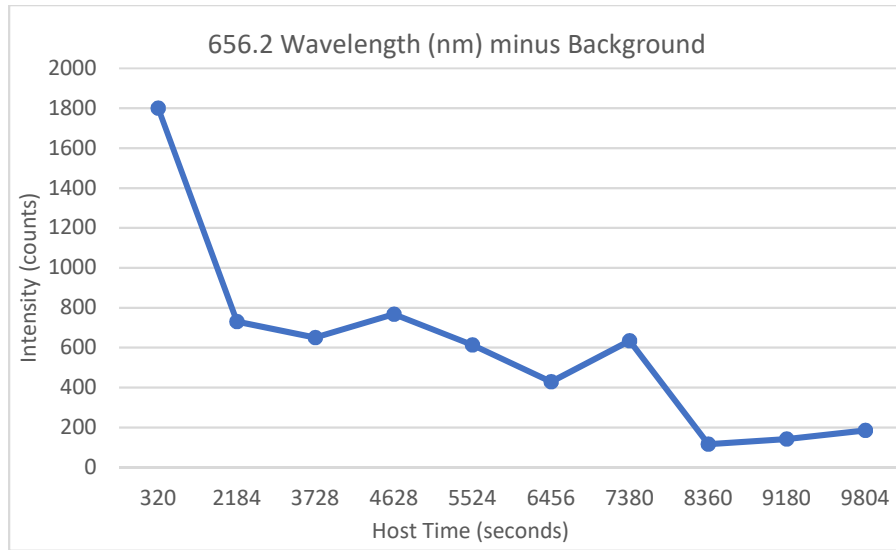


Figure 5.11: Plot of OES data showing decrease in hydrogen (water) content throughout a combined effect FHD test with failed rod and spacer disc.

5.3 Ceria Pellets Used in Failed Rod Testing

Background

Using Cerium Oxide as a proxy for UO₂ avoids contamination of the extensive experimental setup. Cerium oxide has similar properties to UO₂ such as insoluble in water, the same fluorite crystal structure, which is uncommon for oxides and Cerium oxide as similar thermal expansion, thermal diffusivity and heat capacity as UO₂ (See Table 5.4). Ceria as a surrogate material for UO₂ has been drawing more and more attention in recent days in the research community to represent UO₂. In the drying experiments, where one does not wish to contaminate the extensive research facilities to be used, ceria is an excellent surrogate.

Table 5.4. Surrogate Material CeO₂ for UO₂

	UO ₂	CeO ₂
Crystal Structure	Fluorite	Fluorite
Lattice Parameter (Å)	5.47	5.41
Density (g/cm ³)	10.97	7.215
Melting Temperature (°C)	2865	2600
<u>Thermal diffusivity (m²s⁻¹)</u>		
@ 600°K	1.82x10 ⁻⁶	1.96x10 ⁻⁶
@ 1000°K	1.15x10 ⁻⁶	1.15x10 ⁻⁶

Fabrication of CeO₂

The University of Florida undertook the fabrication of ceria oxide pellets to the dimensional specification of Areva Atrium 10, which is the fuel being examined in the drying experiment. The dish on the pellets was produced, however the chamfer was not produced. Optimization of the fabrication process included the varying of several parameters. This included but was not limited to the following:

- Varying sintering conditions
- Die and punch dimensions and surface quality
- Variance of green density and
- Quality of starting powder

Due to the nature of ceramics, final results were highly sensitive to the smallest of changes during the fabrication process. A house of cards is a fitting analogy for the processing of ceramic materials. Starting powder quality is critical to the compaction and sinterability of the pellets. Consideration was taken towards:

- **Purity:** Powder used was 99.99% cerium oxide.
- **Particle size:** Generally, it was determined that the smaller, the better. A smaller particle lowers the sintering temperature required to yield high density. This is critical for cerium oxide, as it easily reduces from (IV) to (III) oxidation states with increases in temperature.
- **Additives:** Binder was tested, however it was found that it did not increase green strength dramatically and therefore was not used. Commercial powder with an average particle size $\leq 1.0 \mu\text{m}$ was used. No additional milling was performed.

Green Pellet Compaction

Formation of density gradients and delamination in the green pellets were early issues in the initial fabrication process that UF resolved by addressing:

- **Die wall smoothness:** It was found that the Die wall required close to mirror finish to reduce friction at the powder to die wall interface.
- **Lubrication:** Zinc stearate and Teflon based lubricating sprays were used on the die wall and punch surfaces to further reduce friction.
- **Powder particle size and quality:** It was found that the powder had to be Fine and free of hard agglomerates.
- **Compaction method:** Single action vs double action

Pressure applied to the powder was found to decrease with the distance from the punch. This response is due to an axial pressure loss due to the shear forces between the powder-to-die-wall interface. It was found that Pellets with an $L/D > 0.5$ should be pressed using the double action method.

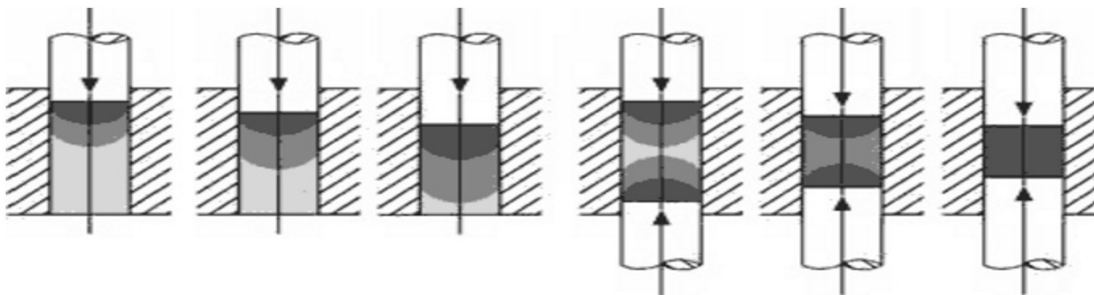


Figure 5.12. Single action (left) and double action (right) die configurations

Pellets were pressed double action at 340 MPa. This fabrication process led to a 60% green density, on average. This procedure also led to both strong green and post sintered pellets. It was found that even slight variance of applied pressure changed the green density, which lead to out-of-tolerance sintered pellets. This occurred because all pellets reach the same density after sintering. If green density isn't controlled, final diameters aren't either.

Sintering

Sintering was performed in a box furnace at normal atmosphere. Controlled atmospheres were tested but were found to be unnecessary or showed negative effects. It was found that there was a small temperature window for achieving high density and minimal reduction. This was found to be in between 1400°C and 1500°C. Temperature above this was found to lead to moderate to severe reduction of the ceria to cerium. The Pellets were sintered in large batches at 1400°C for 10 hours with a heating rate of 200°C/hr. UF used sacrificial ceria powder to line the alumina sintering crucibles to prevent diffusion between the crucible and the pellets.

Delivery of CeO₂ Pellets for Failed Fuel Pin Testing

More than 400 CeO₂ pellets, which were produced at the University of Florida were delivered to the University of South Carolina in January 2016. These pellets were loaded in a failed fuel rod for drying tests. The failure was replicated by drilling a small hole in the fuel pin cladding, where the hole was increased for subsequent tests. The pellets are within dimensional specification for the Areva Atrium 10A and Atrium 10B fuel assemblies. The average dimensional characterization is given in Table 5.5.

Table 5.5. Average density and dimensions

Average Density ($\% \rho_{theoretical}$)	97.5%
Average Diameter	8.682 mm
Average Length	10.310 mm

The pellets show a considerable amount of durability but some slight chipping may occur, however. The pellets were still be handled with care, especially when loading the fuel pin. In addition to measurements, all of the finished pellets were loaded in the sample cladding to confirm proper fitting. Figure 5.13 shows a sample of the finished pellets.



Figure 5.13. Finished pellets and cladding test

One drawback of the pellets is their lack of defects such as cracking and porosity. This is a concern since this is not characteristic of used fuel which will tend to have the opposite of these features. Fabricating pellets that exactly resemble used fuel would be challenging, however it may be possible to produce pellets that have some degree of cracking and porosity while maintaining a good enough strength for repeated handling.

Submersion Tests of Delivered CeO₂ Pellets

Submersion test results for UO₂ and CeO₂. Pellets were submerged in water for 4, 8, 12, and 24 hours then weighed and compared with the initial dry mass. The lack of cracks and surface defects in the CeO₂ pellets prevented absorption of very much moisture. The UO₂ pellets had very minor cracks which may explain the higher amount of absorption in UO₂.

Table 5.6. 4 Hour Submersion

	Initial Mass (g)	Final Mass (g)	Difference (g)
UO ₂	5.51198	5.51246	0.00048
CeO ₂	4.29911	4.29935	0.00024

Table 5.7. 8 Hour Submersion

	Initial Mass (g)	Final Mass (g)	Difference (g)
UO ₂	5.53871	5.53933	0.00062
CeO ₂	4.29868	4.29870	0.00002

Table 5.8. 12 Hour Submersion

	Initial Mass (g)	Final Mass (g)	Difference (g)
UO ₂	5.53937	5.53999	0.00062
CeO ₂	4.24295	4.24330	0.00035

Table 5.9. 24 Hour Submersion

	Initial Mass (g)	Final Mass (g)	Difference (g)
UO ₂	5.52490	5.52618	0.00128
CeO ₂	4.31888	4.31890	0.00002

5.4 FHD Design and Operation

FHD Design

Modifications were made to the experimental design to enable recirculation of helium at pressures between 1000 to 1200 torr and flow rates between 100 to 125 SLPM. Inline gas heaters were added with each capable of up to 1kW and providing an increase of gas temperature of about 50°C (Figure 5.14). These were designed to reach and maintain a recirculating gas temperature of 150°C. Each inline gas heater has an integrated type-K thermocouple. OES and relative humidity measurements already in use for vacuum tests were used to monitor the decreasing water content with drying. Initial tests required excessively long drying times and chamber temperatures were much lower than in vacuum drying tests. This was attributed to the much larger chamber surface area to heated volume (assembly volume) ratio compared with a full-size canister. This is not an issue for vacuum drying tests owing to the greatly reduced heat loss through the chamber walls and piping when under vacuum. However, with FHD, helium is a very effective heat transfer medium and results in a much larger heat loss.

To compensate, the heater rods inside the chamber total output was increased to 3kW to help stem heat loss and raise the test rod temperature to that typical of drying operations. Also, heating tape, thermocouples, and insulation were added to the outside chamber walls to reduce heat loss and maintain a nearly consistent wall temperature of 100°C (see Figure 5.15). Details of thermocouple locations are shown in Section 5.1.

FHD Criteria

For FHD testing, the desiccators were replaced/recycled and in some cases the liquid nitrogen cold trap was used to maintain a low relative humidity after the desiccators. This was measured by relative humidity sensor, HMT2, after the desiccators to keep relative humidity at approximately 0.1% (lower limit). The other relative humidity sensor, HMT1, is located on the test chamber. When this reaches 1% relative humidity, the chamber is isolated and the relative humidity is monitored. When the chamber still contained a significant amount of water, the relative humidity would rebound as shown in Figure 5.16. With drying the rebounds would become smaller (Figure 5.16).

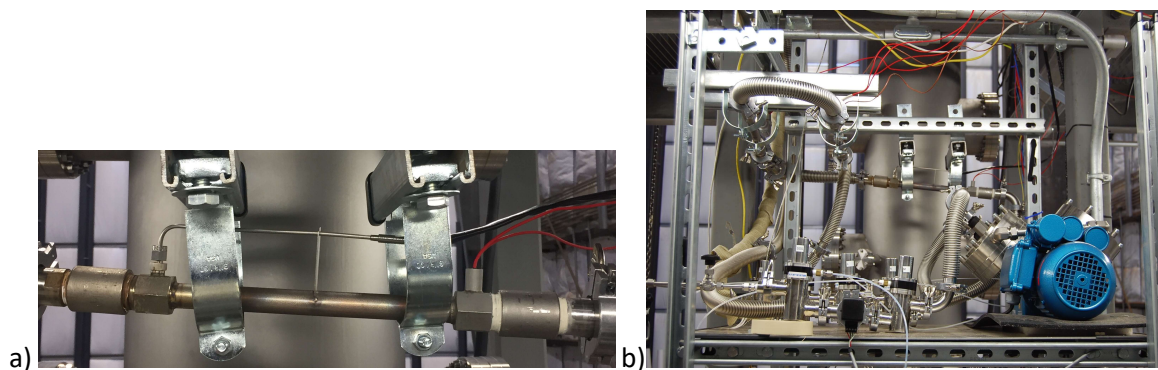


Figure 5.14: Modifications for FHD. a) inline gas heater with integrated thermocouple, b) FHD components with three inline gas heaters and recirculation pump.

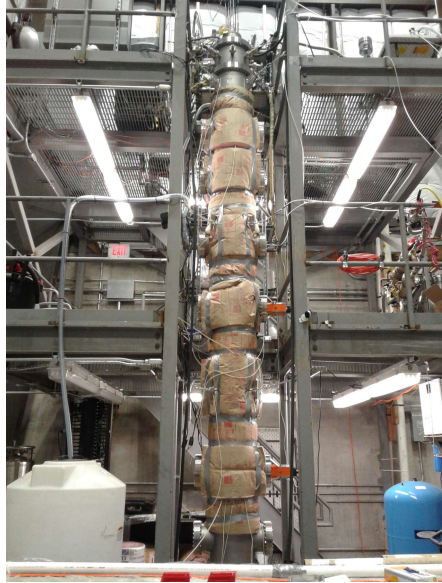


Figure 5.15: Chamber wrapped in insulation. Heating tape and thermocouples under insulation and on outside of the chamber.

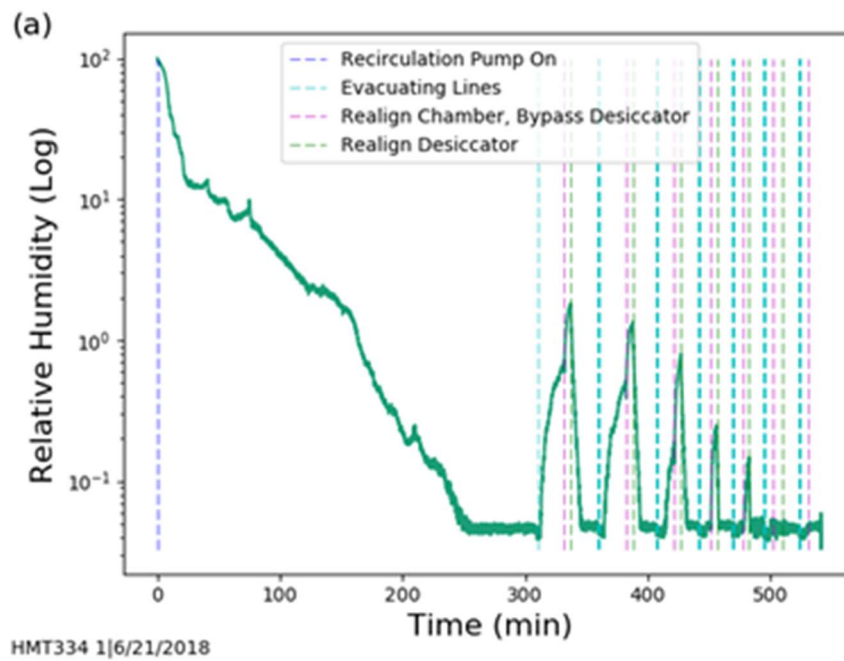


Figure 5.16: Relative humidity measured on the chamber during a FHD test. Note rebounding relative humidity when not dry and decreasing rebounds as the chamber dries.

6. Summary of Results

6.1 Freezing

Testing called for making observations of any freezing that might occur during drying tests. Freezing was noted in two instances: 1) Spacer disc external to the basket and rails, 2) Siphon tube in some vacuum drying tests.

Freezing was noted in the performance of tests involving spacer discs. These features are part of some casks and are horizontally flat metal plates extending from the basket and rails to the canister walls (see Figure 6.1a). Because they are horizontally flat, they may hold some water following blowdown. This feature was simulated by a stainless-steel plate with a back tilted at a slight angle to hold a measured amount of water (about 25cc). Freezing was noted as shown in Figure 6.1. This freezing however did not affect drying ultimately since as long as water (ice) remained in the spacer disc this would melt during the isolation hold and the test would fail the dryness criteria and the evacuation and hold would be repeated until criteria was met.

Freezing was also noted in the siphon tube during some vacuum tests. Initially, the freezing was suspected and later the thermocouple located on the bottom of the chamber near viewport 1 was moved and attached to the bottom of the siphon tube after which freezing was confirmed (see Figure 6.2). It was known that the temperatures at the bottom of the chamber might be expected to be lower than the typical cask. This is owing to the fact that the heated assembly is offset from the bottom of the chamber by a 12-inch pedestal which was required to secure the ends of the heater rods and connect to the electrical ground. Also, the power profile of the heater rods is cosine shaped which concentrates more power at the central chamber height whereas a typical decay heat profile is more flat with a dramatic fall off of power near the ends. To offset the effect of this reduced heat at the chamber bottom, heating tape was added to the outside bottom of the chamber. After this addition, the freezing in the siphon tube was not observed.

6.2 Drying Results

All assembly and chamber features were dried during normal industry procedures except for the failed rod and the bottom of chamber. Test conditions and times were recorded in each test and the remaining water was measured when water was present at the end of a test.

In tests of the failed rod, these met the dryness criteria (vacuum and FHD) even though a minimal amount of water was remaining in the rod. Typically, the failed rod retained between 7 to 12cc (Figure 6.3). As described earlier, heating tape, insulation, and thermocouples were added to the outside chamber wall as a way to control heat loss during FHD and also to be able to prescribe and hold a given wall temperature for more predictable operation. After heating tape and insulation were added to the outside of the chamber, the failed rod was dried in almost all tests. In a few such tests, a small amount of water was measured in the range of 0.5 to 2cc. Thermal images of the failed rod defect hole showed water coming out until reaching pressures between 100 to 50 torr (before heating tape added outside chamber). After heating tape was added, water could be seen coming out typically until around 10 torr. This can be partially explained by the higher failed rod temperature of ~100-130°C in these tests. The retention of water in the failed rod can be understood due to surface tension effects in the tightly

packed rods. Drying the failed rod would also be made difficult since communication between the simulated failure hole and the top or bottom of the rod due to the highly fractured pellets that developed after the first few tests. Additionally, it is expected that the simulated failed rod contains more water than typical since the hold down spring is not fully compressed without proper tooling. The hold down spring is 13 inches uncompressed. Indeed, 40cc of water was injected in the first test and following tests we were only able to put in approximately 30cc of water in a given test indicating about 10cc of water retained.

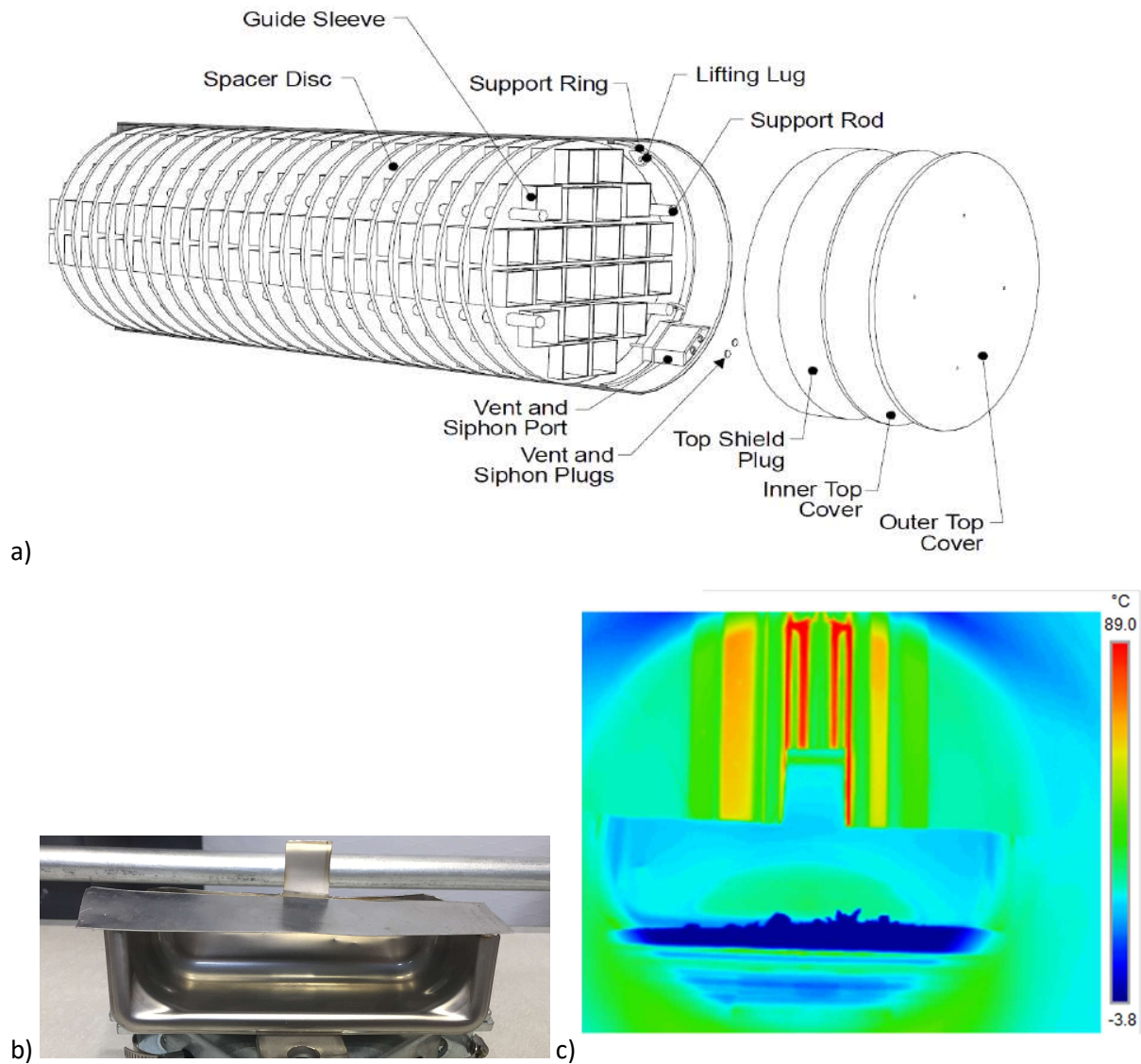


Figure 6.1: a) Some canisters contain spacer discs which are horizontally flat features that can retain water. a) Transnuclear 24PT Dry Storage Canister, b) simulated spacer disc capable of containing approximately 25cc of water. c) thermal image from vacuum drying test showing freezing of water in the simulated spacer disc (note ice crystals forming up the backside of the simulated spacer disc. Note: temperatures shown are in Celsius.

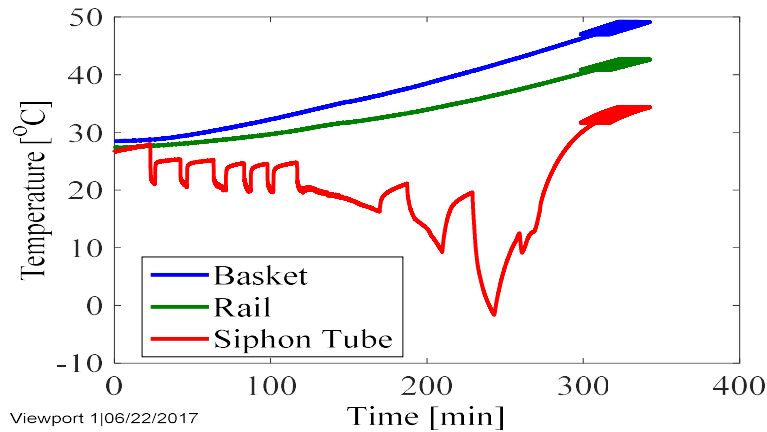


Figure 6.2: Freezing shown in the siphon tube at the bottom of the chamber in combined effect testing before the addition of heating tape to the bottom of the chamber.

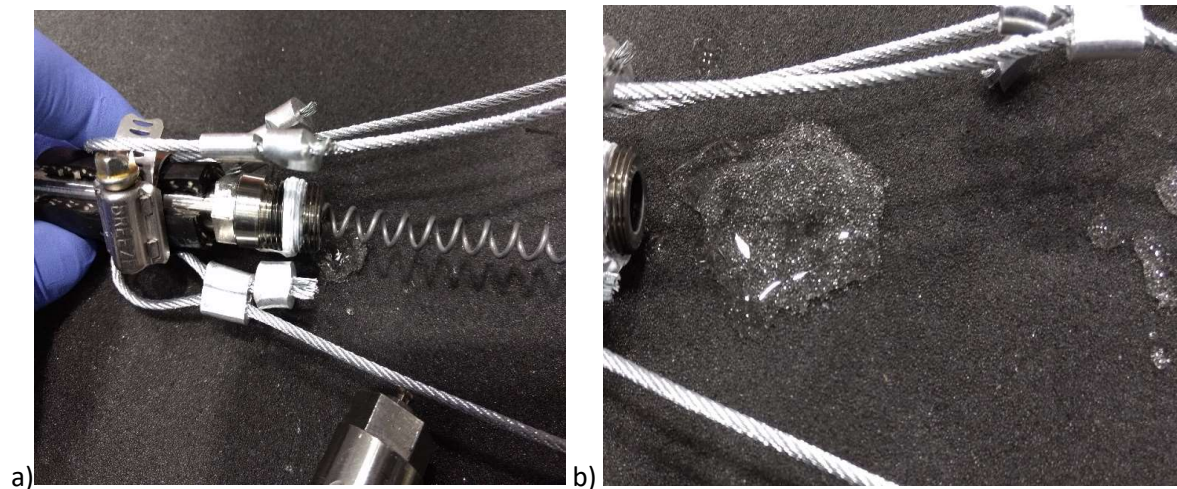


Figure 6.3: Some water (typically 7 to 12 cc) was retained in the failed rod tests while meeting the dryness criteria. Following the addition of heating tape and insulation to outside of the chamber the rod was completely dried in almost all tests.

Water was also shown to be retained at the bottom of the chamber during combined effect testing (both vacuum and FHD) before the addition of heating tape and insulation outside the chamber (see Figure 6.4). This heating tape was first added to the bottom of the test chamber and allowed for better control of temperature in that region since the assembly pedestal is not typical of a cask and means the bottom is further from the heat source. Also, heater rods have a cosine shaped distribution so there is less heat near the bottom than otherwise typical. Once the heating tape and insulation was added, complete dryness of the chamber was achieved in every type of FHD and vacuum test.

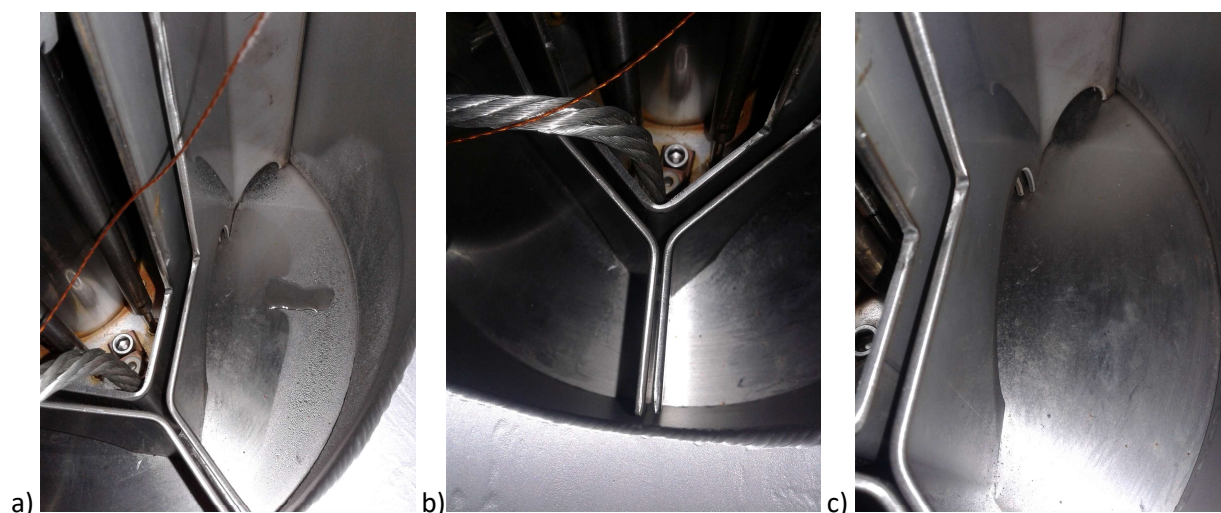


Figure 6.4: Some water (few cc) was typically retained at the bottom of the chamber in combined tests before heating tape was added to the bottom of the chamber to offset the somewhat lower than typical heat generation at the bottom. Far left photo shows typical moisture remaining after testing before the addition of heating tape and insulation, whereas the far right shows typical dry results after.

6.3 Range of Peak Test Rod Temperatures for Different Types of Tests

The range of peak test rod temperatures for different types of tests is shown in Table 6.1. These are the ranges of the peak temperature which is observed near the end of the test. These test rod temperatures are taken from the thermal images recorded through the viewport imaging the particular feature for this type of test. This is not necessarily and typically is not the peak temperature in the thermal image since rods immediately adjacent to the heater rods are hotter.

Table 6.1: Range of Peak Test Rod Temperatures for Different Types of Tests

Test Type	Range of Test Rod Peak Temperature
Vacuum Single Effect High Power	105°C - 115°C
Vacuum Single Effect Low Power	85°C - 100°C
Vacuum Combined High Power	130°C - 145°C
Vacuum Combined Low Power	95°C - 110°C
Forced Circulation Single Effect High Power	155°C - 190°C
Forced Circulation Single Effect Low Power	90°C - 105°C
Forced Circulation Combined High Power	145°C - 160°C

6.4. Maximum Heater Rod and Chamber Thermocouple Temperatures by Test Type

The drying data was surveyed to extract the average maximum heater rod and chamber temperatures for each type of test. This data is shown in Table 6.2. It is notable that all the rod temperatures were less than the regulatory limit of 400°C. Maximum rod temperature is related to power level (simulated decay heat) of course but also to the length of the test since rods are increasing in temperature under vacuum and with recirculation of hot helium gas. As can be seen, temperatures for tests that resulted in dry conditions were generally higher than those for not dry conditions. This data is useful in developing predictive models for drying.

Table 6.2: Average maximum value for a given rod position or chamber location by type of drying test.

Vacuum, Single Effect, Low Power, Dry						
	Heater Rod 1	Heater Rod 2	Heater Rod 3	Heater Rod 5	Heater Rod 6	Heater Rod 7
PWR	168.0	156.7	105.9	174.0	163.6	164.3
BWR	172.5	171.7	122.3	176.4	168.6	167.9
Failed Rod Spacer Disc	174.9	176.3	116.6	178.5	172.3	163.7

Vacuum, Single Effect, Low Power, Not Dry						
	Heater Rod 1	Heater Rod 2	Heater Rod 3	Heater Rod 5	Heater Rod 6	Heater Rod 7
PWR						
*BWR	177.7	177.2	131.9	181.3	176.3	174.0
Failed Rod Spacer Disc	169.2	170.9	108.8	172.7	163.9	124.8

*From one test

Vacuum, Single Effect, High Power, Dry						
	Heater Rod 1	Heater Rod 2	Heater Rod 3	Heater Rod 5	Heater Rod 6	Heater Rod 7
PWR	302.0	292.4	180.3	299.5	285.8	281.6
BWR	340.6	340.3	239.2	349.6	327.1	328.2
*Failed Rod	284.6	284.1	159.1	293.7	273.5	270.6
Spacer Disc	316.4	316.0	212.1	325.9	305.7	306.3

*From one test

Vacuum, Single Effect, High Power, Not Dry						
	Heater Rod 1	Heater Rod 2	Heater Rod 3	Heater Rod 5	Heater Rod 6	Heater Rod 7
PWR						
BWR						
Failed Rod Spacer Disc	310.7	301.1	206.9	305.7	311.0	289.4

Vacuum, Combined, High Power, Dry						
	Heater Rod 1	Heater Rod 2	Heater Rod 3	Heater Rod 5	Heater Rod 6	Heater Rod 7
PWR	355.0	355.0	267.3	362.4	344.2	345.1
BWR	308.0	347.7	263.5	358.0	353.8	344.0
Failed Rod	333.8	333.4	241.6	342.5	332.5	325.0
Spacer Disc	321.3	347.4	263.7	357.1	354.4	342.7

Vacuum, Combined, High Power, Not Dry						
	Heater Rod 1	Heater Rod 2	Heater Rod 3	Heater Rod 5	Heater Rod 6	Heater Rod 7
PWR						
**BWR	340.8	340.3	250.5	349.1	330.1	330.9
*Failed Rod	361.9	361.7	282.4	369.8	349.3	351.6
*Spacer Disc	361.9	361.7	282.4	369.8	349.3	351.6

*From one test; **Rod Dry each time but chamber not dry

Table 6.2: Average maximum value for a given rod position or chamber location by type of drying test.

FHD, Single Effect, 1kW Power, Not Dry*						
	Heater Rod 1	Heater Rod 2	Heater Rod 3	Heater Rod 5	Heater Rod 6	Heater Rod 7
PWR	171.1	172.1	141.9	173.7	174.0	172.6
BWR						
Failed Rod						
Spacer Disc						

*limited tests at lower power prior to mods to achieve realistic drying temperatures during FHD

FHD, Single Effect, 3kW Power, Dry						
	Heater Rod 1	Heater Rod 2	Heater Rod 3	Heater Rod 5	Heater Rod 6	Heater Rod 7
PWR	376.6	379.4	312.3	370.8	368.0	367.7
BWR	351.2	354.6	291.8	349.4	349.4	347.0
Failed Rod	357.0	360.4	296.7	353.3	347.5	346.7
Spacer Disc	359.2	362.5	299.3	357.4	357.4	354.0

FHD, Single Effect, 3kW Power, Not Dry						
	Heater Rod 1	Heater Rod 2	Heater Rod 3	Heater Rod 5	Heater Rod 6	Heater Rod 7
PWR	344.8	348.7	283.5	339.9	343.6	334.4
BWR	338.9	342.6	280.0	336.3	337.4	334.0
Failed Rod	344.6	348.7	284.7	343.0	341.4	335.5
Spacer Disc	346.0	350.0	286.6	346.3	344.2	343.1

FHD, Combined, 3kW Power, Dry						
	Heater Rod 1	Heater Rod 2	Heater Rod 3	Heater Rod 5	Heater Rod 6	Heater Rod 7
PWR	363.1	370.2	306.0	363.7	371.7	361.4
BWR	354.7	361.0	299.1	353.5	361.0	345.6
Failed Rod	333.0	337.6	265.1	336.5	334.2	329.9
Spacer Disc	358.2	365.3	302.2	356.5	365.9	347.5

FHD, Combined, 3kW Power, Not Dry						
	Heater Rod 1	Heater Rod 2	Heater Rod 3	Heater Rod 5	Heater Rod 6	Heater Rod 7
PWR						
BWR	326.8	331.5	269.1	326.9	329.1	328.2
Failed Rod	317.3	323.7	258.7	318.4	320.7	312.4
Spacer Disc	314.1	319.6	256.0	314.8	316.4	314.2

Table 6.2: Average maximum value for a given rod position or chamber location by type of drying test.

Vacuum, Single Effect, Low Power, Dry						
	Heater Rod 8	Heater Rod 9	Heater Rod 10	Heater Rod 11	Heater Rod 12	VP1 Basket
PWR	154.7	114.0	106.4	162.5	163.6	28.7
BWR	168.5	132.4	123.8	163.9	168.5	40.7
Failed Rod Spacer Disc	157.3	125.9	106.7	156.3	164.5	45.1

Vacuum, Single Effect, Low Power, Not Dry						
	Heater Rod 8	Heater Rod 9	Heater Rod 10	Heater Rod 11	Heater Rod 12	VP1 Basket
PWR						
*BWR	175.0	141.9	133.7	169.8	175.9	34.8
Failed Rod Spacer Disc	115.6	111.7	57.1	148.7	152.3	35.8

*From one test

Vacuum, Single Effect, High Power, Dry						
	Heater Rod 8	Heater Rod 9	Heater Rod 10	Heater Rod 11	Heater Rod 12	VP1 Basket
PWR	293.4	222.5	184.5	280.4	282.5	53.7
BWR	331.5	261.1	244.3	329.2	326.2	47.8
*Failed Rod	276.8	173.9	165.2	272.7	273.5	58.7
Spacer Disc	308.5	234.1	217.5	305.5	304.5	44.2

*From one test

Vacuum, Single Effect, High Power, Not Dry						
	Heater Rod 8	Heater Rod 9	Heater Rod 10	Heater Rod 11	Heater Rod 12	VP1 Basket
PWR						
BWR						
Failed Rod Spacer Disc	224.1	214.3	86.9	279.7	283.4	44.1

Vacuum, Combined, High Power, Dry						
	Heater Rod 8	Heater Rod 9	Heater Rod 10	Heater Rod 11	Heater Rod 12	VP1 Basket
PWR	346.3	289.6	271.9	340.0	343.4	76.4
BWR	343.8	296.4	277.5	341.8	346.3	77.7
Failed Rod	264.8	260.4	247.7	324.3	326.0	70.4
Spacer Disc	325.1	292.1	275.3	340.8	344.5	76.7

Vacuum, Combined, High Power, Not Dry						
	Heater Rod 8	Heater Rod 9	Heater Rod 10	Heater Rod 11	Heater Rod 12	VP1 Basket
PWR						
**BWR	332.3	273.4	255.1	327.9	328.9	49.9
*Failed Rod	352.9	305.9	286.2	367.1	350.3	52.8
*Spacer Disc	352.9	305.9	286.2	367.1	350.3	52.8

*From one test; **Rod Dry each time but chamber not dry

Table 6.2: Average maximum value for a given rod position or chamber location by type of drying test.

FHD, Single Effect, 1kW Power, Not Dry*						
	Heater Rod 8	Heater Rod 9	Heater Rod 10	Heater Rod 11	Heater Rod 12	VP1 Basket
PWR	176.2	148.1	142.6	161.9	174.5	34.6
BWR						
Failed Rod						
Spacer Disc						

*limited tests at lower power prior to mods to achieve realistic drying temperatures during FHD

FHD, Single Effect, 3kW Power, Dry						
	Heater Rod 8	Heater Rod 9	Heater Rod 10	Heater Rod 11	Heater Rod 12	VP1 Basket
PWR	368.4	320.4	304.0	340.3	363.1	81.8
BWR	348.5	304.1	289.1	322.2	344.7	85.2
Failed Rod	305.0	298.5	289.3	334.7	344.6	78.2
Spacer Disc	355.2	311.6	295.1	327.0	350.9	83.2

FHD, Single Effect, 3kW Power, Not Dry						
	Heater Rod 8	Heater Rod 9	Heater Rod 10	Heater Rod 11	Heater Rod 12	VP1 Basket
PWR	341.8	293.1	279.6	312.3	336.3	78.5
BWR	337.4	296.2	277.3	310.5	333.6	71.8
Failed Rod	298.0	291.8	283.1	333.2	335.3	77.1
Spacer Disc	302.3	296.8	286.2	337.6	339.2	78.6

FHD, Combined, 3kW Power, Dry						
	Heater Rod 8	Heater Rod 9	Heater Rod 10	Heater Rod 11	Heater Rod 12	VP1 Basket
PWR	372.8	324.4	313.0	343.2	369.5	98.0
BWR	363.4	315.9	306.5	336.8	361.2	84.4
Failed Rod	338.0	281.3	271.6	333.5	337.3	83.0
Spacer Disc	368.1	318.6	309.8	338.7	364.8	96.2

FHD, Combined, 3kW Power, Not Dry						
	Heater Rod 8	Heater Rod 9	Heater Rod 10	Heater Rod 11	Heater Rod 12	VP1 Basket
PWR						
BWR	331.8	283.5	272.9	307.8	330.9	57.9
Failed Rod	326.4	274.7	265.3	319.0	325.6	51.8
Spacer Disc	315.1	271.7	260.5	299.3	320.1	47.7

Table 6.2: Average maximum value for a given rod position or chamber location by type of drying test.

Vacuum, Single Effect, Low Power, Dry						
	VP1 Rail	/P1 Siphon Tub	VP2 Basket	VP2 Rail	VP2 Channel	VP3 Basket
PWR	26.8	23.9	46.1	39.2	62.0	75.2
BWR	41.0	36.8	64.7	56.9	77.1	91.7
Failed Rod Spacer Disc	45.8	53.9	70.9	68.7	83.5	90.6

Vacuum, Single Effect, Low Power, Not Dry						
	VP1 Rail	/P1 Siphon Tub	VP2 Basket	VP2 Rail	VP2 Channel	VP3 Basket
PWR						
*BWR	30.8	22.5	56.7	46.8	75.0	92.3
Failed Rod Spacer Disc	32.0	57.5	51.4	70.3	84.6	72.0

*From one test

Vacuum, Single Effect, High Power, Dry						
	VP1 Rail	/P1 Siphon Tub	VP2 Basket	VP2 Rail	VP2 Channel	VP3 Basket
PWR	53.8	50.8	112.6	105.7	133.5	149.5
BWR	40.3	25.1	107.1	82.6	137.3	169.9
*Failed Rod	52.8	127.2	126.9	140.6	137.8	116.9
Spacer Disc	37.9	30.1	87.0	66.4	126.7	153.3

*From one test

Vacuum, Single Effect, High Power, Not Dry						
	VP1 Rail	/P1 Siphon Tub	VP2 Basket	VP2 Rail	VP2 Channel	VP3 Basket
PWR						
BWR						
Failed Rod Spacer Disc	37.4	106.0	91.1	134.4	160.3	131.8

Vacuum, Combined, High Power, Dry						
	VP1 Rail	/P1 Siphon Tub	VP2 Basket	VP2 Rail	VP2 Channel	VP3 Basket
PWR	72.7	58.9	144.2	127.1	179.3	208.7
BWR	72.8	56.7	150.6	133.9	185.4	211.8
Failed Rod	63.8	140.9	131.6	168.8	196.4	174.8
Spacer Disc	72.3	87.4	146.9	148.2	196.6	209.0

Vacuum, Combined, High Power, Not Dry						
	VP1 Rail	/P1 Siphon Tub	VP2 Basket	VP2 Rail	VP2 Channel	VP3 Basket
PWR						
**BWR	42.8	30.8	101.9	79.2	143.0	180.0
*Failed Rod	41.0	122.2	97.0	163.5	206.6	168.0
*Spacer Disc	41.0	122.2	97.0	163.5	206.6	168.0

*From one test; **Rod Dry each time but chamber not dry

Table 6.2: Average maximum value for a given rod position or chamber location by type of drying test.

FHD, Single Effect, 1kW Power, Not Dry*						
	VP1 Rail	/P1 Siphon Tube	VP2 Basket	VP2 Rail	VP2 Channel	VP3 Basket
PWR	34.1	30.4	62.6	56.9	70.8	106.6
BWR						
Failed Rod						
Spacer Disc						

*limited tests at lower power prior to mods to achieve realistic drying temperatures during FHD

FHD, Single Effect, 3kW Power, Dry						
	VP1 Rail	/P1 Siphon Tube	VP2 Basket	VP2 Rail	VP2 Channel	VP3 Basket
PWR	79.0	77.7	159.5	146.2	186.1	251.2
BWR	83.5	81.7	156.9	144.8	180.0	235.2
Failed Rod	75.9	158.4	145.9	180.9	246.4	226.7
Spacer Disc	80.9	78.8	164.6	151.8	187.4	248.7

FHD, Single Effect, 3kW Power, Not Dry						
	VP1 Rail	/P1 Siphon Tube	VP2 Basket	VP2 Rail	VP2 Channel	VP3 Basket
PWR	76.5	93.0	150.8	139.1	172.6	233.7
BWR	70.3	79.6	135.9	123.6	155.6	219.9
Failed Rod	72.4	155.3	143.8	176.4	234.6	214.8
Spacer Disc	72.3	158.2	146.6	179.6	235.4	215.2

FHD, Combined, 3kW Power, Dry						
	VP1 Rail	/P1 Siphon Tube	VP2 Basket	VP2 Rail	VP2 Channel	VP3 Basket
PWR	98.3	85.6	198.9	188.7	218.4	258.3
BWR	84.4	72.7	170.5	159.7	193.2	245.7
Failed Rod	66.2	164.6	156.3	184.7	218.7	201.1
Spacer Disc	89.7	144.7	186.9	196.3	228.4	246.9

FHD, Combined, 3kW Power, Not Dry						
	VP1 Rail	/P1 Siphon Tube	VP2 Basket	VP2 Rail	VP2 Channel	VP3 Basket
PWR						
BWR	57.5	64.6	124.0	112.1	143.6	204.7
Failed Rod	166.9	114.2	102.2	130.6	196.1	173.4
Spacer Disc	121.2	85.1	101.6	109.8	158.8	178.4

Table 6.2: Average maximum value for a given rod position or chamber location by type of drying test.

Vacuum, Single Effect, Low Power, Dry						
	VP3 Rail	VP3 Channel	VP4 Basket	VP4 Rail	VP4 Channel	VP5 Basket
PWR	62.2	105.9	72.0	60.6	101.5	58.1
BWR	77.7	121.8	86.0	73.3	115.3	70.1
Failed Rod Spacer Disc	86.5	112.5	82.6	80.0	104.1	70.0

Vacuum, Single Effect, Low Power, Not Dry						
	VP3 Rail	VP3 Channel	VP4 Basket	VP4 Rail	VP4 Channel	VP5 Basket
PWR						
*BWR	74.2	126.7	87.4	71.0	121.1	68.4
Failed Rod Spacer Disc	111.8	78.8	67.4	105.1	64.8	60.3

*From one test

Vacuum, Single Effect, High Power, Dry						
	VP3 Rail	VP3 Channel	VP4 Basket	VP4 Rail	VP4 Channel	VP5 Basket
PWR	127.9	193.8	135.4	113.5	180.8	108.3
BWR	131.3	231.3	161.2	125.0	220.6	122.6
*Failed Rod	186.8	118.9	97.3	170.4	94.9	85.1
Spacer Disc	117.9	214.1	145.6	112.7	203.3	110.3

*From one test

Vacuum, Single Effect, High Power, Not Dry						
	VP3 Rail	VP3 Channel	VP4 Basket	VP4 Rail	VP4 Channel	VP5 Basket
PWR						
BWR						
Failed Rod Spacer Disc	208.5	148.7	121.2	196.4	115.5	102.7

Vacuum, Combined, High Power, Dry						
	VP3 Rail	VP3 Channel	VP4 Basket	VP4 Rail	VP4 Channel	VP5 Basket
PWR	177.0	260.8	193.7	161.5	246.1	155.4
BWR	180.2	263.3	197.1	164.6	249.2	158.3
Failed Rod	242.6	180.9	158.3	227.7	146.3	136.7
Spacer Disc	206.3	243.7	193.9	191.0	222.3	159.7

Vacuum, Combined, High Power, Not Dry						
	VP3 Rail	VP3 Channel	VP4 Basket	VP4 Rail	VP4 Channel	VP5 Basket
PWR						
**BWR	143.0	240.0	172.3	138.0	229.2	131.4
*Failed Rod	264.9	198.0	161.7	253.0	154.6	139.6
*Spacer Disc	264.9	198.0	161.7	253.0	154.6	139.6

*From one test; **Rod Dry each time but chamber not dry

Table 6.2: Average maximum value for a given rod position or chamber location by type of drying test.

FHD, Single Effect, 1kW Power, Not Dry*						
	VP3 Rail	VP3 Channel	VP4 Basket	VP4 Rail	VP4 Channel	VP5 Basket
PWR	93.5	120.9	107.5	96.4	115.8	91.9
BWR						
Failed Rod						
Spacer Disc						

*limited tests at lower power prior to mods to achieve realistic drying temperatures during FHD

FHD, Single Effect, 3kW Power, Dry						
	VP3 Rail	VP3 Channel	VP4 Basket	VP4 Rail	VP4 Channel	VP5 Basket
PWR	227.6	252.3	250.6	229.3	247.0	226.6
BWR	214.8	246.2	232.0	213.2	236.5	206.6
Failed Rod	244.0	243.8	224.9	233.0	219.0	211.8
Spacer Disc	228.5	254.1	243.9	225.8	243.2	217.7

FHD, Single Effect, 3kW Power, Not Dry						
	VP3 Rail	VP3 Channel	VP4 Basket	VP4 Rail	VP4 Channel	VP5 Basket
PWR	214.2	236.6	230.1	212.4	225.6	204.8
BWR	198.1	231.3	218.3	198.6	221.6	191.5
Failed Rod	245.6	230.3	212.1	233.8	203.0	197.5
Spacer Disc	251.1	230.1	212.1	238.4	202.0	197.1

FHD, Combined, 3kW Power, Dry						
	VP3 Rail	VP3 Channel	VP4 Basket	VP4 Rail	VP4 Channel	VP5 Basket
PWR	242.9	276.6	250.5	234.1	263.0	223.0
BWR	226.9	271.9	240.9	224.1	259.2	217.2
Failed Rod	246.6	209.9	192.6	233.4	185.1	180.6
Spacer Disc	250.9	262.0	239.6	242.7	241.5	219.8

FHD, Combined, 3kW Power, Not Dry						
	VP3 Rail	VP3 Channel	VP4 Basket	VP4 Rail	VP4 Channel	VP5 Basket
PWR						
BWR	182.6	231.8	202.2	182.8	222.6	175.8
Failed Rod	224.2	195.2	175.7	214.8	167.3	163.7
Spacer Disc	192.8	203.7	179.2	189.0	185.4	159.7

Table 6.2: Average maximum value for a given rod position or chamber location by type of drying test.

Vacuum, Single Effect, Low Power, Dry					
	VP5 Rail	VP5 Channel	VP6 Basket	VP6 Rail	VP6 Channel
PWR	53.3	82.1	44.0	41.0	60.0
BWR	64.8	94.3	55.8	52.6	71.3
Failed Rod Spacer Disc	70.6	88.0	60.2	60.2	75.8

Vacuum, Single Effect, Low Power, Not Dry					
	VP5 Rail	VP5 Channel	VP6 Basket	VP6 Rail	VP6 Channel
PWR					
*BWR	61.4	97.2	50.0	45.7	69.7
Failed Rod Spacer Disc	86.3	53.1	50.9	66.5	102.6

*From one test

Vacuum, Single Effect, High Power, Dry					
	VP5 Rail	VP5 Channel	VP6 Basket	VP6 Rail	VP6 Channel
PWR	98.3	146.6	84.8	79.7	109.0
BWR	105.1	176.9	83.0	73.1	123.8
*Failed Rod	138.1	68.3	62.7	97.8	92.3
Spacer Disc	95.7	163.1	75.4	67.1	114.5

*From one test

Vacuum, Single Effect, High Power, Not Dry					
	VP5 Rail	VP5 Channel	VP6 Basket	VP6 Rail	VP6 Channel
PWR					
BWR					
Failed Rod Spacer Disc	158.1	78.9	71.3	110.5	90.4

Vacuum, Combined, High Power, Dry					
	VP5 Rail	VP5 Channel	VP6 Basket	VP6 Rail	VP6 Channel
PWR	139.5	204.1	110.3	100.6	149.5
BWR	142.6	207.1	108.0	98.3	148.8
Failed Rod	187.0	103.4	97.1	133.8	92.7
Spacer Disc	162.1	178.1	110.3	113.7	130.5

Vacuum, Combined, High Power, Not Dry					
	VP5 Rail	VP5 Channel	VP6 Basket	VP6 Rail	VP6 Channel
PWR					
**BWR	117.9	185.3	89.6	81.2	131.1
*Failed Rod	207.7	105.6	96.5	149.2	
*Spacer Disc	207.7	105.6	96.5	149.2	

*From one test; **Rod Dry each time but chamber not dry

Table 6.2: Average maximum value for a given rod position or chamber location by type of drying test.

FHD, Single Effect, 1kW Power, Not Dry*					
	VP5 Rail	VP5 Channel	VP6 Basket	VP6 Rail	VP6 Channel
PWR	88.5	98.4	77.7	75.3	78.2
BWR					
Failed Rod					
Spacer Disc					

*limited tests at lower power prior to mods to achieve realistic drying temperatures during FHD

FHD, Single Effect, 3kW Power, Dry					
	VP5 Rail	VP5 Channel	VP6 Basket	VP6 Rail	VP6 Channel
PWR	218.7	220.7	193.7	190.1	183.1
BWR	200.9	207.6	176.7	173.3	168.2
Failed Rod	210.0	186.2	183.6	170.5	96.0
Spacer Disc	212.1	213.5	185.9	183.0	173.0

FHD, Single Effect, 3kW Power, Not Dry					
	VP5 Rail	VP5 Channel	VP6 Basket	VP6 Rail	VP6 Channel
PWR	200.1	199.8	174.2	172.0	162.2
BWR	186.5	194.4	163.2	159.9	157.0
Failed Rod	203.4	171.4	168.7	163.5	97.7
Spacer Disc	205.3	170.6	167.8	165.1	99.5

FHD, Combined, 3kW Power, Dry					
	VP5 Rail	VP5 Channel	VP6 Basket	VP6 Rail	VP6 Channel
PWR	219.9	228.4	199.0	196.9	190.3
BWR	214.4	224.8	192.7	190.4	185.0
Failed Rod	200.1	161.3	158.6	162.4	100.7
Spacer Disc	221.5	213.3	197.1	190.2	152.5

FHD, Combined, 3kW Power, Not Dry					
	VP5 Rail	VP5 Channel	VP6 Basket	VP6 Rail	VP6 Channel
PWR					
BWR	172.1	188.5	150.2	146.7	150.5
Failed Rod	181.7	142.3	138.4	144.3	101.2
Spacer Disc	167.1	155.7	133.9	135.5	143.2

7. Modeling of Used Fuel Drying by Vacuum and Gas Circulation for Dry Cask Storage

Introduction

The modeling effort aims to conduct simulation of the complete 3D mock assembly with a multi-phase multi-physics model. The early effort in modelling approach focused on the completion of building 3D geometry of the assembly in COMSOL and solved for energy to have a cursory/superficial/brief understanding of the effect of heater rods on the test rod considering a constant evaporative heat loss. However, to simulate the experiment it is necessary to solve continuity, momentum balance, energy and species transport and have a strong coupling among them with varying (depending on pressure and temperature) evaporative heat and mass transfer. Furthermore, to emulate the actual scenario, a moving boundary condition must be prescribed at the liquid gas interface. So, along the aforementioned physics, a moving mesh or deformed geometry physics needs to be solved in numerical modeling. This modeling effort looks forward to including these features in the numerical model to simulate the experiment.

Mathematical Model:

This effort proposes a numerical model comprised of coupled mass, momentum and energy conservation equations. A species transport equation needs to be solved for resolving the phase change and the associated transport from the liquid to the vapor phase. With the simplest of approximations, energy transport in the liquid film can be assumed to be only due to conduction. The temperature in both the phases is to be resolved assuming a thermal equilibrium at the liquid-gas phase interface. For brevity, only the important relations and boundary conditions are provided at this section. The details of the conservation equation are provided in the later section where the test geometry is explained.

a) Evaporative mass transfer:

The mass transfer from free liquid surface due to evaporation is obtained from the net evaporative flux described by the modified Hertz-Knudsen (HK) relation [1, 2].

$$\dot{m}_{evap(flux)} = \sigma \sqrt{\frac{M}{2\pi RT_L}} (P_s(T_L) - P_v) \quad (1)$$

where, $\dot{m}_{evap(flux)}$ is the net evaporative mass transfer per unit area, M is the molecular weight, R is the universal gas constant, P_s is the saturation pressure, P_v is the partial vapor pressure. T_L is the interface temperature of the liquid side and σ is the accommodation coefficient.

The partial vapor pressure P_v is calculated from the mass fraction of vapor in helium-water vapor mixture which is found by solving the species transport equation. The saturation vapor pressure P_s is a function of interface temperature in the liquid side and can be expressed by Antoine equation [3]:

$$\log(P_s) = A - \frac{B}{T_L} \quad (2)$$

where, $A = 20.386$ and $B = 5132$ for water for temperature between 1°C to 99°C .

So, the flux boundary condition for the species transfer equation at liquid-gas interface can be expressed as below:

$$\bar{n} \cdot \dot{m}_{evap(flux)} = \rho_{mix} D_k \nabla Y_k - \rho_{mix} \bar{u} Y_k \quad (3)$$

b) Evaporative heat transfer:

The evaporative heat loss from liquid gas interface is to be prescribed as one of the boundary conditions of the energy equation and it is described by following equation:

$$q_w - q_g = \dot{Q}_L \quad (4)$$

where, q_w is the heat flux in the liquid phase having contribution from conduction alone, q_g is the heat flux in the gas phase having contribution from both conductive and convective fluxes and \dot{Q}_L is the evaporative heat loss and is expressed as:

$$\dot{Q}_L = \dot{m}_{evap(flux)} h_{fg} \quad (5)$$

where, h_{fg} is the latent heat of evaporation.

c) Moving boundary:

Since the HK relation is expressed in terms of interface properties it is important to locate the liquid-gas interface correctly. The film recedes vertically with time changing the spatial position of liquid-vapor interface. Therefore, a moving mesh technique has been implemented to

track the receding film. An Arbitrary Lagrangian-Eulerian (ALE) [4] technique with a Laplace smoothing approach is considered. In ALE method, the following equations are solved:

$$\frac{\partial^2}{\partial X^2} \frac{\partial x}{\partial t} + \frac{\partial^2}{\partial Y^2} \frac{\partial x}{\partial t} = 0 \quad (6)$$

$$\frac{\partial^2}{\partial X^2} \frac{\partial y}{\partial t} + \frac{\partial^2}{\partial Y^2} \frac{\partial y}{\partial t} = 0 \quad (7)$$

where, X and Y are material frame coordinates and x and y are mesh coordinates. Since the dissipation is occurring in the y direction only, the mesh displacement along x direction is zero. Mesh displacement along the y direction at time t is calculated by, $\Delta y = v_{mesh} t$, where, v_{mesh} is the moving mesh velocity that can be calculated from the evaporative mass transfer expression, $v_{mesh} = \dot{m}_{evap}/(\rho_w A_s)$.

Approach to numerical modeling

The proposed model consists of continuity, momentum, species and energy balance with a moving liquid-gas interface. So, before putting all of these physics together in the full 3D geometry model, we consider a single column of water, representative of the test rod, and add the physics interface one by one to acquire better insights and finally putting all these together in the full 3D geometry. A chronological addition of individual physics in a simple single rod model is described below as an approach to unravel the numerical modeling.

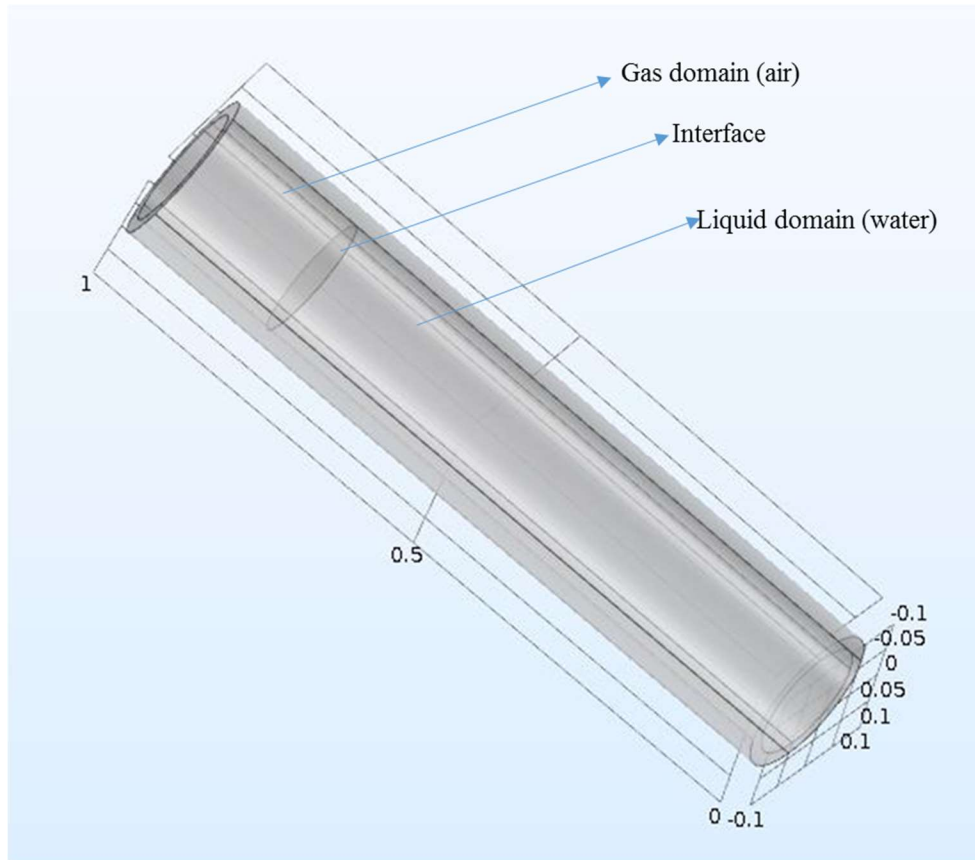


Figure 7.1: Single rod geometry

In the effort of approaching to the modeling first a single column consisting of two distinct domains is considered (Figure 7.1).

For the first case of numerical experiment/exercise, the functionality of moving mesh interface is checked with a species transport equation and a constant mass transfer rate at the interface for a no-flow isothermal system (Figure 7.2)

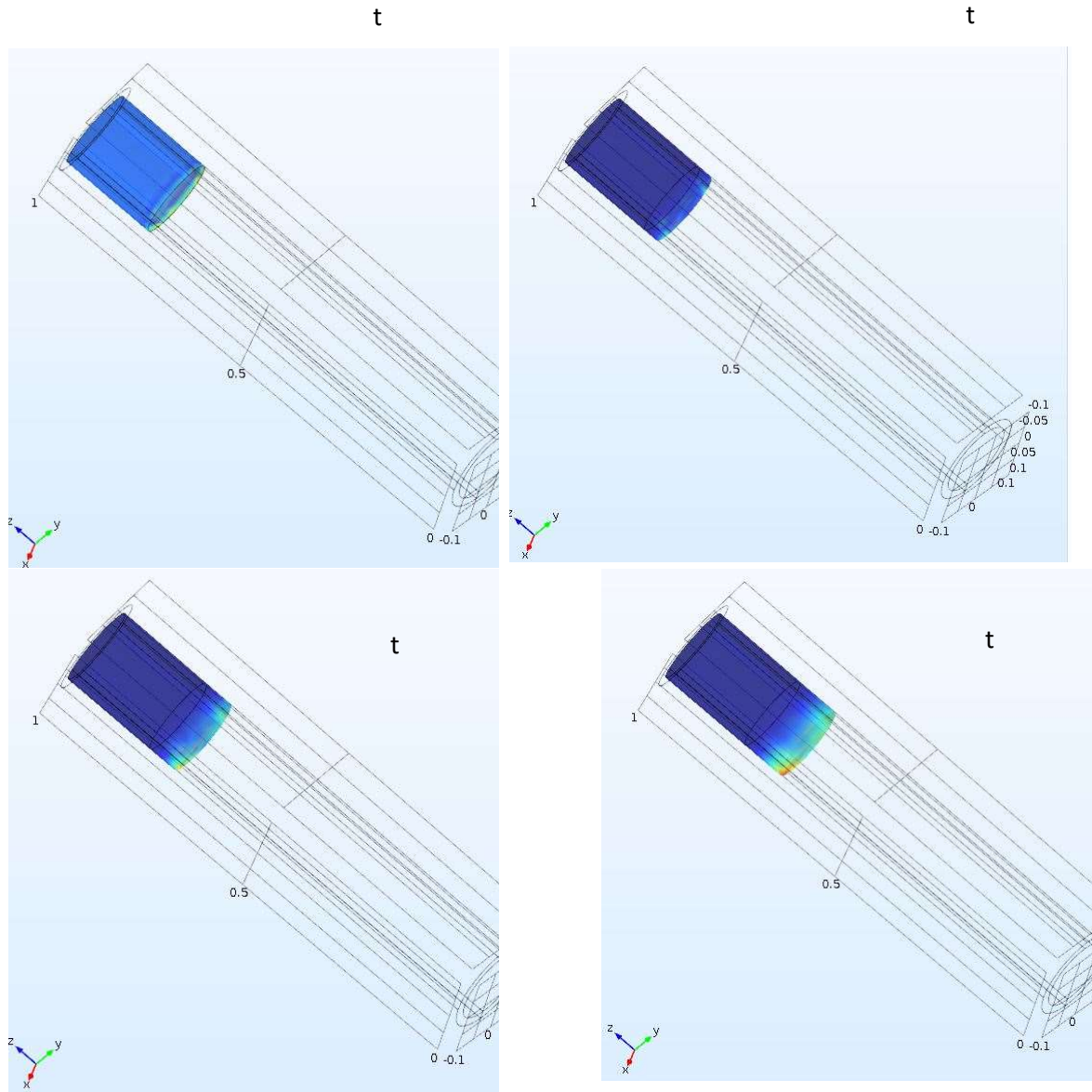


Figure 7.2: Temporal evolution of water vapor distribution in the gas phase and the receding of liquid-gas interface for a constant evaporation rate in a no-flow isothermal system.

In the next step, energy equation is added to this simple model, prescribing a constant heat flux at the bottom and an evaporative loss term at the interface. In this case, evaporation rate is expressed as a function of temperature to check the functionality of a varying mass transfer rate instead of a constant one. An unsteady water mass distribution of water vapor has been achieved (Figure 7.3).

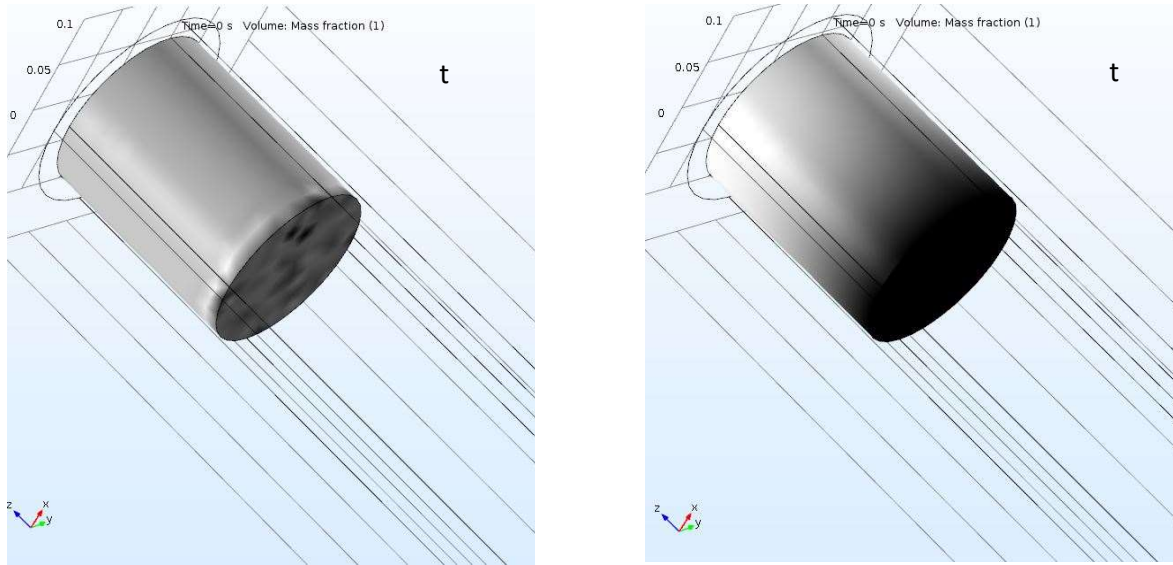


Figure 7.3: Temporal evolution of water vapor distribution in the gas phase for a varying evaporation rate in a no-flow system

Figure 7.3 confirms that it is possible to incorporate evaporation rate as a function of necessary variable. However, the figure does not give the visual confirmation of the receding of the water level, but it is confirmed via a magnified animation that the boundary is moving which has been showed in one of the group meetings.

The numerical investigation of the drying process is a multidimensional multi-physics analysis. The system is composed of fluid dynamics, heat transfer and species transport and all of them are affecting each other. In other words, they are strongly coupled and we need to solve them simultaneously. Our first attempt was to look closely into the physics and understand which parameter/physics is triggered or suppressed by other parameters/physics. So, first we constructed a simple geometry to get confidence on the simulation result of this multi-physics study. We conducted simulation of a single hollow cylinder system consisting of two-phase domains: liquid (water), gas (helium and water vapor). To take account of the heater rod around, we prescribed 'a' heat flux along the wall as a boundary condition. To emulate the experimental pressure variance, we prescribed the pressure reading from the experiment directly as an outlet boundary condition of the system. We incorporated species transfer in gas domain where evaporating water has been prescribed as a boundary source term in the species conservation equation. Navier-Stokes equation has been solved in the gas domain and the flow is driven basically due to the pressure difference. The liquid medium has been considered as a solid, so only conduction is considered through liquid water as a heat transfer process.

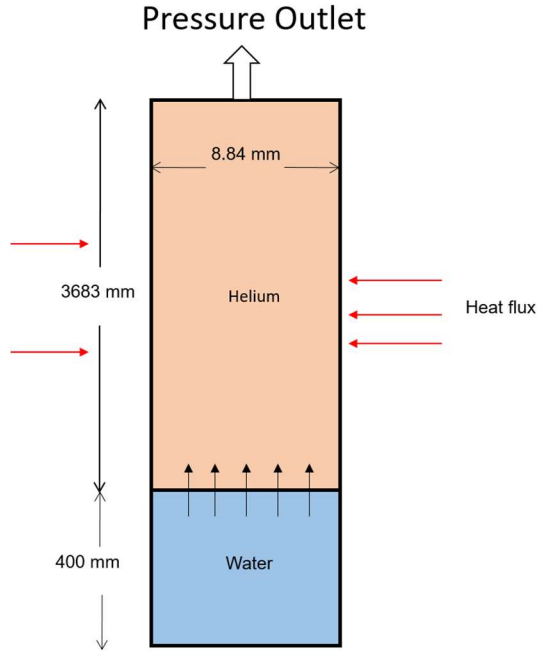


Figure 7.4: Two-dimensional single rod geometry

The conservation equation for the averaged mass is described by mass continuity, conservation of momentum and energy conservation and has the following form as described below. A species conservation equation is employed to resolve the transport of the vapor in the gas domain resulting from the phase change process.

$$\frac{\partial}{\partial t}(\rho_{mix}) + \nabla \cdot (\rho_{mix} \bar{u}) = 0 \quad (8)$$

$$\frac{\partial}{\partial t}(\rho_{mix} \bar{u}) + \nabla \cdot (\rho_{mix} \bar{u} \bar{u}) = -\nabla p + \nabla \cdot \tau \quad (9)$$

$$\frac{\partial}{\partial t}(\rho_{mix} C_p T) + \nabla \cdot (\rho_{mix} C_p \bar{u} T) = -\nabla \cdot q \quad (10)$$

$$\frac{\partial}{\partial t}(\rho_{mix} Y_k) + \nabla \cdot (\rho_{mix} \bar{u} Y_k) = \nabla \cdot (\rho_{mix} D_k \nabla Y_k) \quad (11)$$

where, ρ_{mix} is the mixture density of helium and water vapor in gaseous domain, τ is the shear stress tensor, \bar{u} is the velocity vector, p is the pressure, C_p is the specific heat capacity of the mixture, Y_k is the mass fraction of water vapor in helium-water vapor mixture and D_k is the mass diffusivity of water molecules into air. The energy equation in the liquid phase is expressed in the following form by only considering transport due to conduction:

$$\frac{\partial}{\partial t}(\rho_w C_{p,s} T) = \nabla \cdot (k_w \nabla T) \quad (12)$$

where, ρ_w , $C_{p,s}$ and k_w is the density, specific heat capacity and conductivity of liquid water respectively.

Our philosophy is to conduct numerical studies on this simple geometry to acquire better understanding of the physics, and then marching towards three-dimensional simulation.

As mentioned, we took the pressure reading from the experiments and prescribed this as a boundary condition (varying with time) at the outlet. The following studies have been conducted based on the pressure reading acquired on the 3rd July, 2017 experiment.

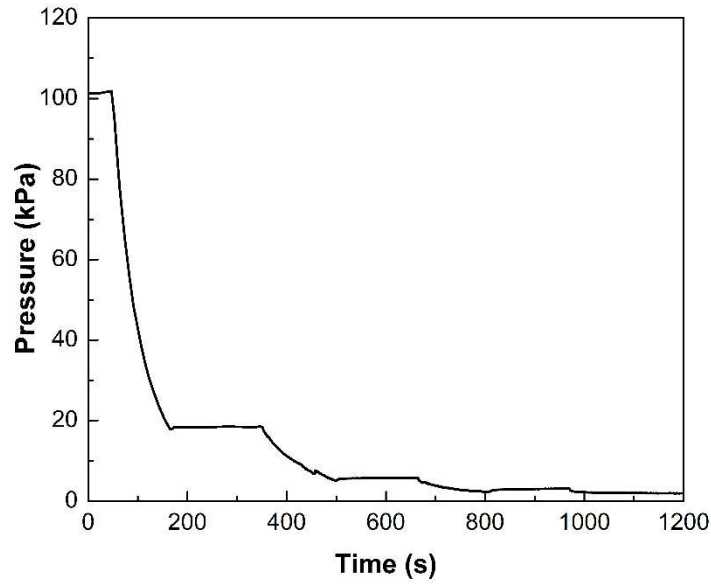


Figure 7.5: Prescribed pressure boundary condition at outlet

As an effort to understand the behavior of the system subjected to a pressure driven flow, we are interested to see the nature of evaporation flux, interface temperature and mass fraction. Figure 7.6 describes the interface temperature as a response to the given pressure boundary condition as a function of time. As we can see, the interface temperature decreases with the pressure drop, and then increases during the period when the pressure is held constant. The first drastic fall of the temperature is a direct consequence of a sudden pressure drop which triggers the evaporation at the very first get go. So, evaporative cooling is reducing the local temperature. This trend is then disrupted by the change of pressure profile. During the period when the pressure is kept almost constant, the pressure difference that drives the flow is minimize. In other word, physically, the system is not undergoing a vacuum process in this period. Therefore, the system is experiencing a ‘kind of’ no-flow condition. And as discussed, the species transport and heat transfer is closely tied with momentum transport, at no-flow condition, species transport is

hindered or diminished, which directly affects the evaporation flux. In physical sense, the evaporation is minimized during this period. So, evaporative cooling cannot compensate the heat coming from the wall (as a heat flux boundary condition emulating the effect of heater rod) and consequently the temperature

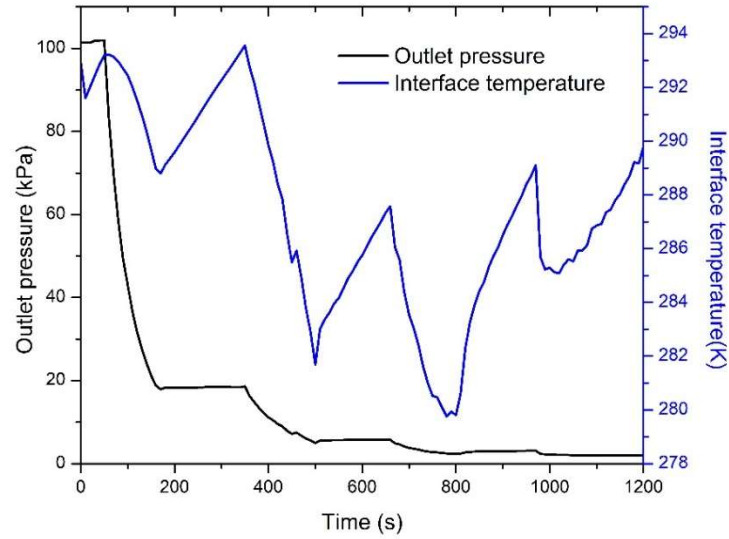


Figure 7.6: Temporal evolution of interface temperature under a prescribed time varying pressure boundary condition

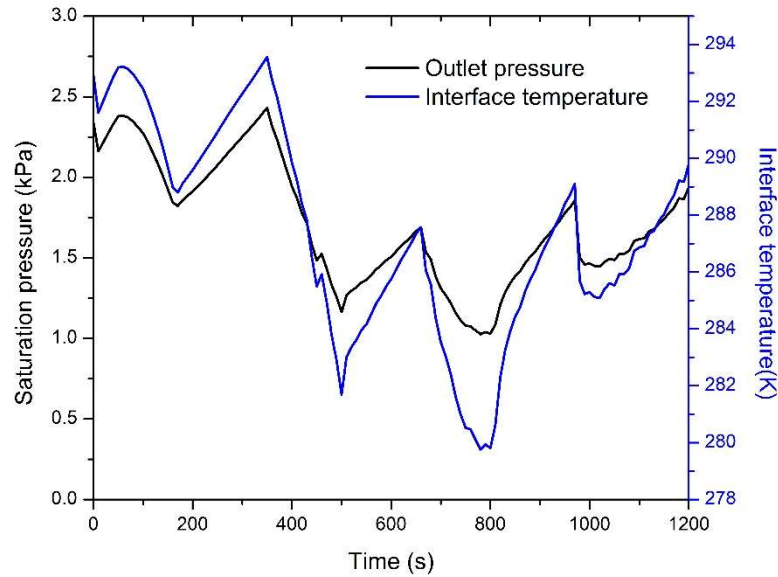


Figure 7.7: Temporal evolution of Saturation pressure as interface temperature changes with time

increases. At this point, we need to recall the definition of Hertz-Knudsen evaporation flux from Eq. 1. It is a function of local temperature and the difference between saturation pressure (at that temperature) and vapor pressure. Figure 7.7 represents the behavior of saturation pressure as temperature changes with time. Following the Antoine equation (Eq. 2), the saturation pressure increases with temperature and vice versa. Now, with the increase of temperature, the saturation pressure increases, hence, the difference between saturation pressure and vapor pressure also increases. This difference will reach a pivotal point where the evaporation will be triggered again. As the evaporative cooling starts to grow dominant, it over-compensates the heat input and consequently reduces the temperature. This explanation is further supported by the evaporation flux profile which has been articulated below.

The evaporation mass flux is plotted against time to investigate its response with pressure variation. The horizontal axis starts from 200 second. We will have a closer look from 0 to 200 second in later section because the initial profile needs special attention. Evaporation mass flux profile showed in Figure 7.8 is consistent with prior discussion. As mentioned, a boosted evaporation is observed in temperature profile during pressure reduction. This is also evident in the evaporation flux profile as well. Besides, during the period when pressure is being held a quasi-constant value, the evaporation mass flux is reduced which is also consistent with the interpretation of Figures 7.6 and 7.7. Now, evaporation mass flux exhibits abrupt ups and down, especially during the pressure-hold period. That is partly because, evaporation mass flux is a function of difference between saturation pressure and vapor pressure. During this period of attention, there is a competition between domain pressure, vapor pressure and saturation pressure. So, evaporation takes places in a back and forth attitude which is exhibited by the abrupt ‘zigzag’ curve in Figure 7.8. During vacuum process, helium is gradually being replaced by water vapor in the gas phase of the vessel. It can be observed in Figure 7.9.

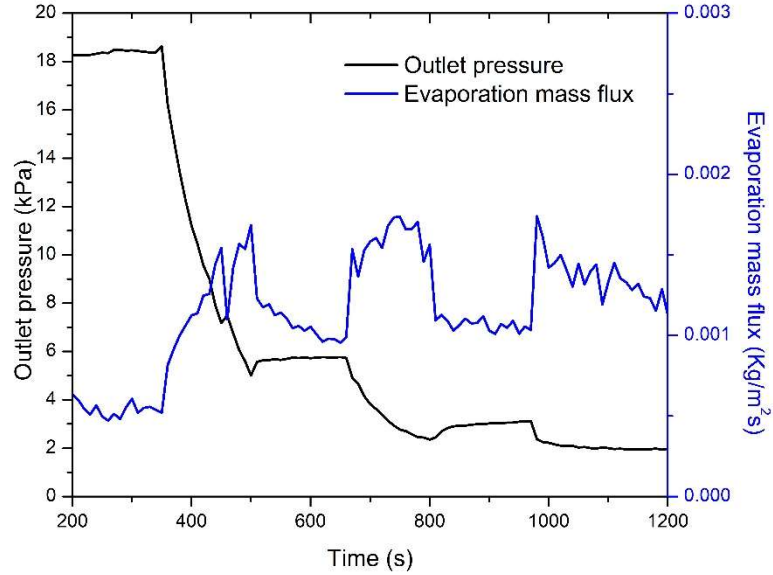


Figure 7.8: Temporal evolution of Saturation pressure as interface temperature changes with time

Figure 7.9 shows that mole fraction of helium is decreasing as that of water vapor is increasing. Since helium is heavier than water, it is more likely to be pulled out in vacuum process. However, this plot raises question, specially near initial and final time. It is expected that the mole fraction of water will reach/tend to ~ 1 asymptotically. In any phase change phenomena, evaporation occurs vigorously initially and then it withers away since the local temperature is reduced due to the evaporation itself. So, even though Figure 7.9 qualitatively confirm the mass conservation, we were expecting mole fraction of water would ramp up exponentially at the beginning and then reach a plateau near a value of 1 asymptotically. This triggers the necessity to have a closer look on evaporation mass flux at early stage which is depicted in Figure 7.10.

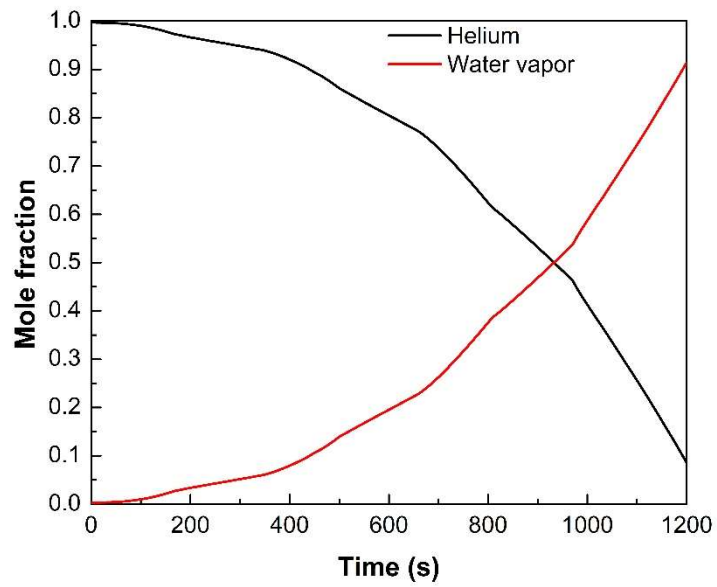


Figure 7.9: Average mole fraction profile with time

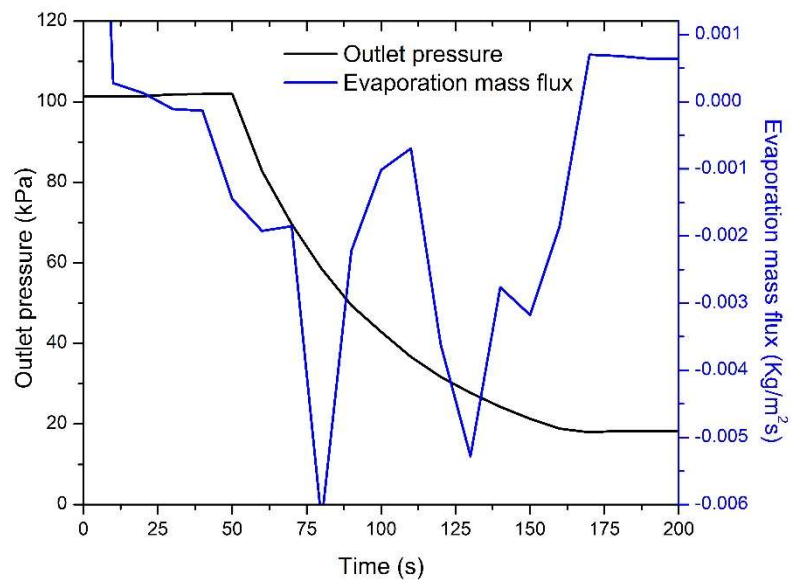


Figure 7.10: Evaporation mass flux at early stage

Surprisingly, a ‘negative’ mass flux is observed during the first pressure reduction period. To investigate this, different between cylinder pressure and the outlet pressure is plotted in Figure 7.11.

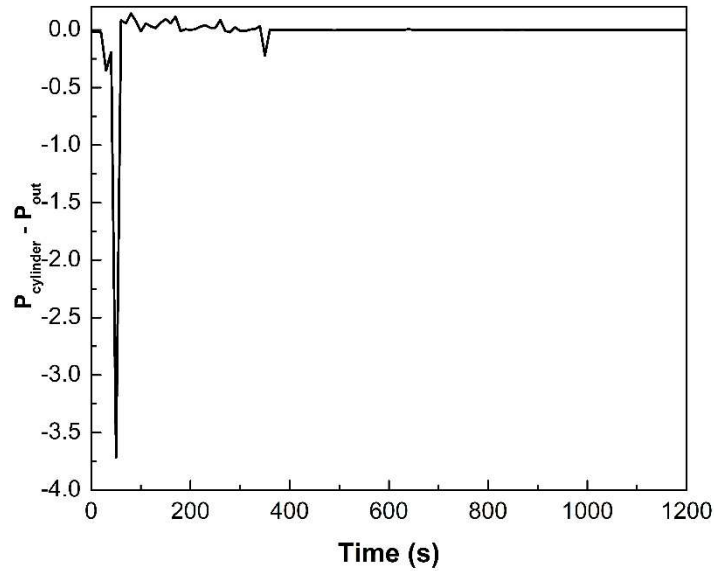


Figure 7.11: Evaporation mass flux at early stage

As evident in Figure 7.10, a negative pressure difference occurs at early stage which indicates a backflow at the outlet. This is the reason a negative mass flux is observed in that period. This triggers the necessity of analyzing the effectiveness using a pressure profile as a boundary condition here. Pressure is a scalar quantity, and the CFD solver would satisfy the continuity based on the prescribed pressure boundary condition irrespective outflow or backflow. This ponders the necessity of inserting the boundary condition in terms of mass outflow rate which would technically satisfy the continuity without the emergence of a backflow situation.

We started with a very simplified geometry shown in Figure 7.12 to check the effect of mass flow rate boundary condition. This is a single-phase flow with no inlet and a prescribed flow rate boundary condition at outlet.

Prescribed flow rate



Figure 7.12: Test geometry

To understand the physics and nature of the flow, we conducted simulation with four different cases of prescribed flow rate: constant flow rate (case 1), flow rate linearly decreasing

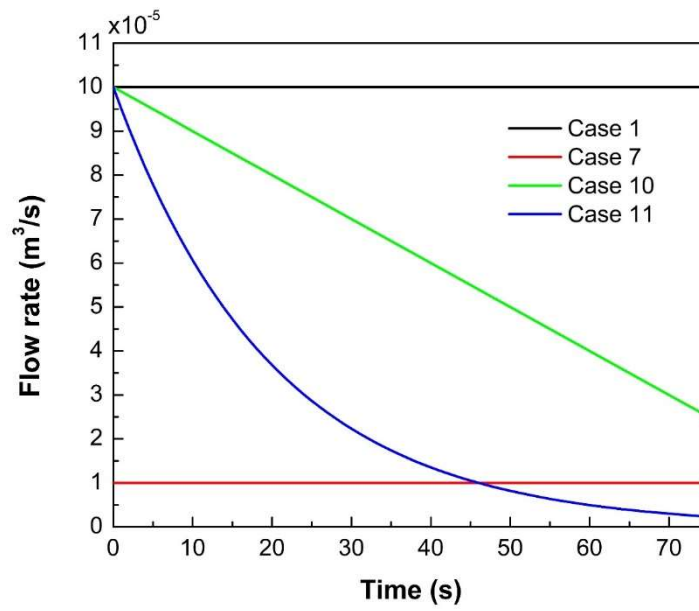


Figure 7.13: Prescribed flow rates for test simulation

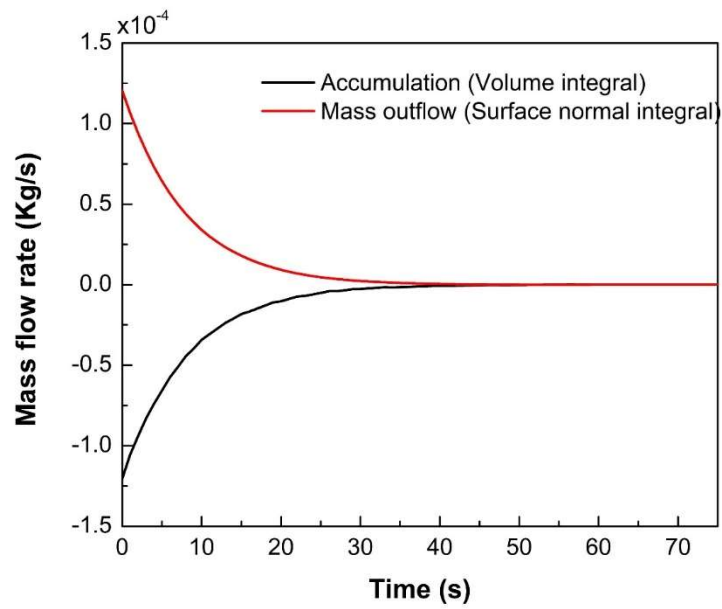
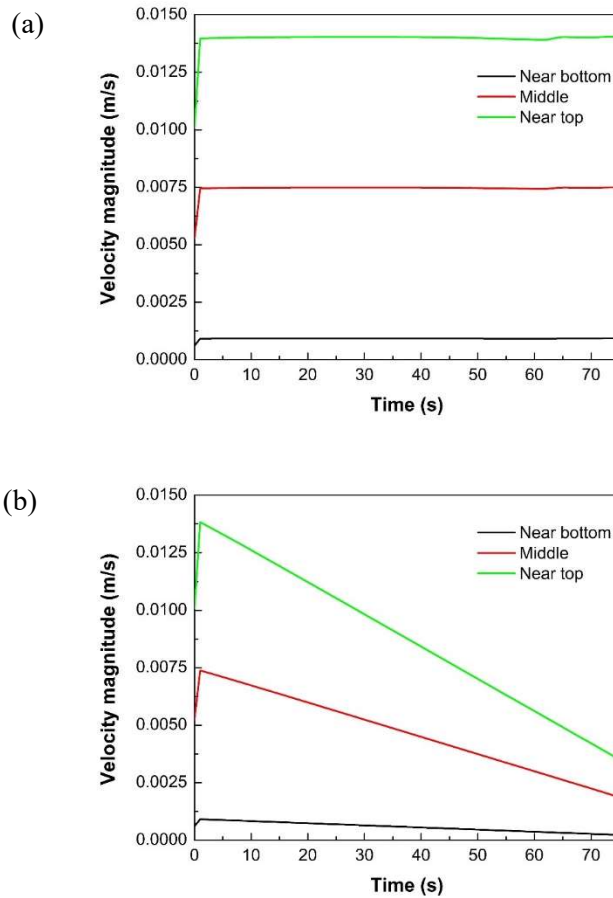


Figure 7.14: Confirmation of conservation of continuity equation

with time (case 10), flow rate exponentially decreasing with time (case 11), and a smaller constant flow rate (case 7). The cases are depicted in Figure 7.13. Figure 7.14 depicts that continuity has been satisfied in the simulation represented by the following equation:

$$\int \left(\frac{\partial \rho}{\partial t} dV \right) + \int \rho \mathbf{u} \cdot \mathbf{n} dS = 0 \quad (13)$$

To check the consistency of the velocity magnitude with prescribed flow rate conditions, we picked 3 different points in the domain, near bottom, at the middle and near top. As it is shown in Figure 7.15, in all the cases velocity magnitude is highest at outlet and lowest at the inlet. This is because of the fact that at bottom, no slip boundary condition has been prescribed. It is also found that, for constant flow rate case, the velocity magnitude at each location remain constant, whereas, for linearly decreasing flow rate, the velocity magnitude decreases linearly and for exponentially decreasing flow rate, the velocity magnitude decreases exponentially with time. So, it is evident that the velocity behaves with prescribed flow rate with consistency.



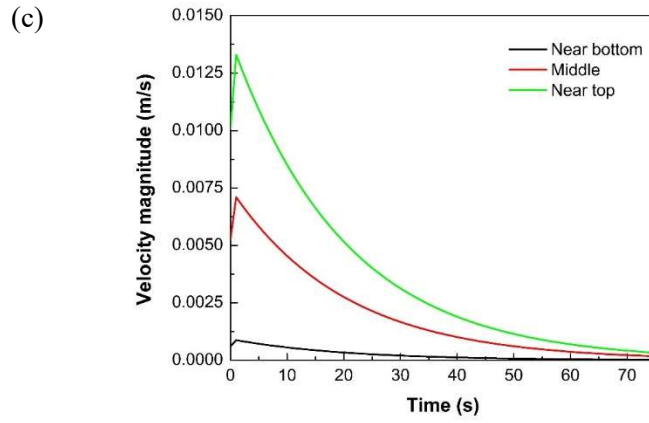
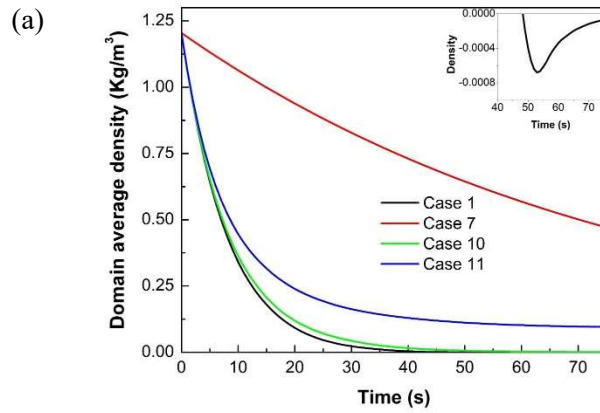


Figure 7.15: Velocity magnitude with time at different location for (a) constant flow rate (b) linearly decreasing flow rate (c) exponentially decreasing flow rate.

We examined the change of average density and pressure of the domain and the mass outflow rate.



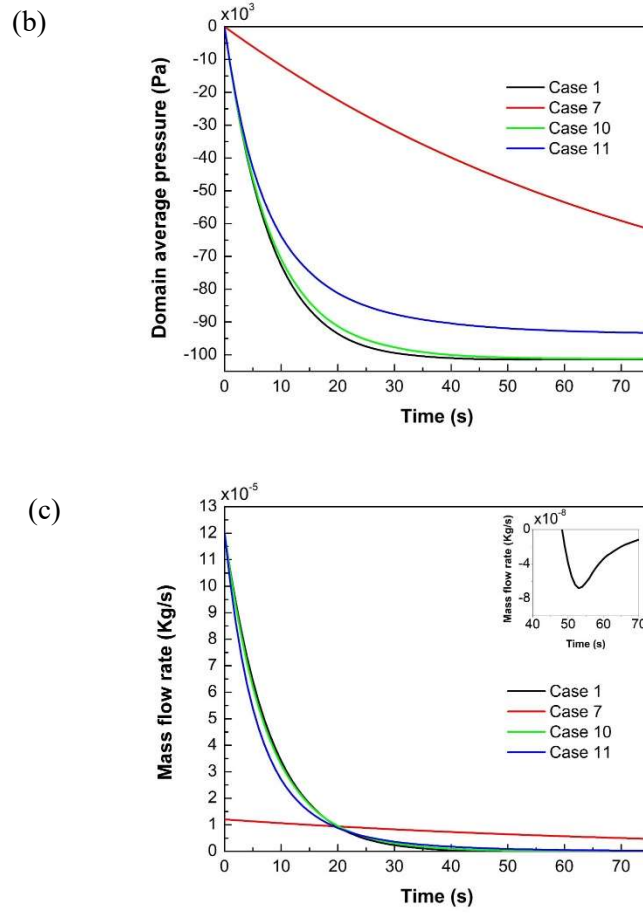


Figure 7.16: Change of (a) density (b) pressure and (c) mass outflow rate with time for different flow rates.

Figure 7.16 depicts the change of domain average density and pressure and overall mass outflow rate with time. Interestingly, for all kind of the flow rates, we are seeing the change of this variables are exponential with time. One might get perplexed by the fact that even with the constant and linearly decreasing flow rate, exponential behavior is observed. This can be explained as follows. In classical ‘large discharge tank’ system, the change of pressure over time is found to be exponentially decreasing with time. The analytical solution is given here briefly:

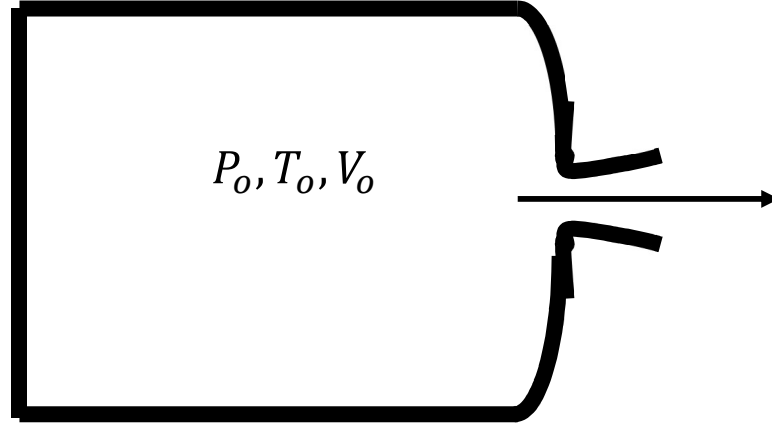


Figure 7.17: Large air discharge tank system

$$\frac{\partial m_{cv}}{\partial t} = -m_e$$

$$\frac{\partial}{\partial t}(\rho_o V) = -m_e$$

$$\frac{\partial}{\partial t} \left(\frac{P_o}{RT} V \right) = -m_e$$

$$\frac{\partial}{\partial t} \left(\frac{P_o}{RT} V \right) = -m_e$$

$$\frac{\partial}{\partial t}(P_o) = -\frac{m_e}{V} RT$$

From Compressible flow:

$$m_e \sim \frac{p_o A^*}{\sqrt{T_o}} \quad [A^* \text{ is the throat area}]$$

$$\frac{\partial}{\partial t}(P_o) = -KP_o$$

$$\frac{\partial P_o}{P_o} = -Kt$$

$$P_o = Ae^{-Kt}$$

So, our current problem can be considered as an analogous system like a large discharge tank system. In large discharge tank system, there is no spatial variation of pressure inside the tank, but a temporal variation of pressure and density is observed. In vacuum drying process, the pressure and density also behave the same way as they do in the large discharge tank system. This

unravels the ostensibly appeared conundrum of finding similar pattern of these variables even with different type of flow rates.

Since we gained confidence on the acquired numerical results, therefore we added all the other relevant physics i.e., heat transfer and species transport in two phase (gas: helium, liquid: water) arrangement. In order to save the computational time, we considered a small scale computational domain (Figure 7.18) compared to our previous domain (Figure 7.4). As an initial attempt, a constant evaporation mass flux at the liquid-gas interface and a constant heat flux at wall have been prescribed.

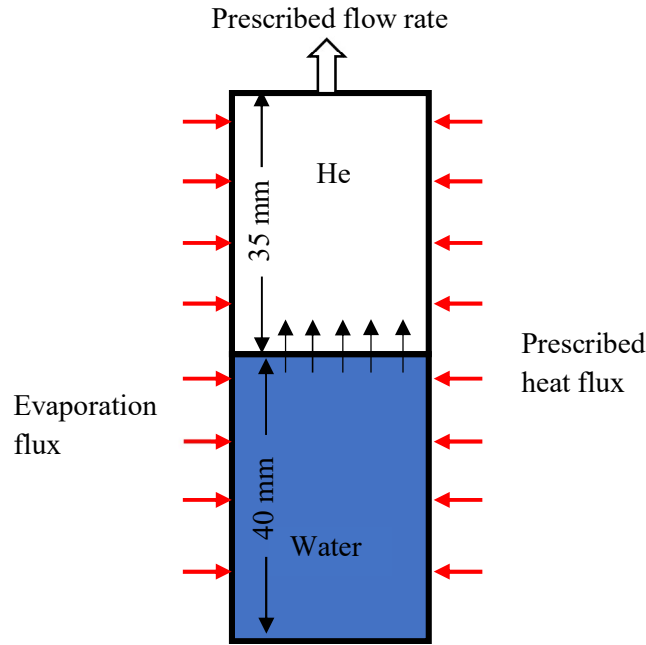


Figure 7.19: 2D computational domain.

Figure 7.19 (a) shows that the average density of the gas phase domain exhibits exponential decay with time as observed in large discharge tank system which has been explained above. Next, we observed the centerline mass fraction distribution of helium and water vapor from liquid-gas interface ($y=40$ mm) to the outlet ($y=76$ mm). Figure 7.19 (b) shows that the water vapor mass fraction is maximum near the interface, because water and vapor is generated at the interface and then diffuses and convected towards the exit. With time, the mass fraction of water is increasing and vice versa for helium since helium is more likely to be pumped out of the system owing to having lower density and at the same time water vapor is being generated from the system at liquid-gas interface.

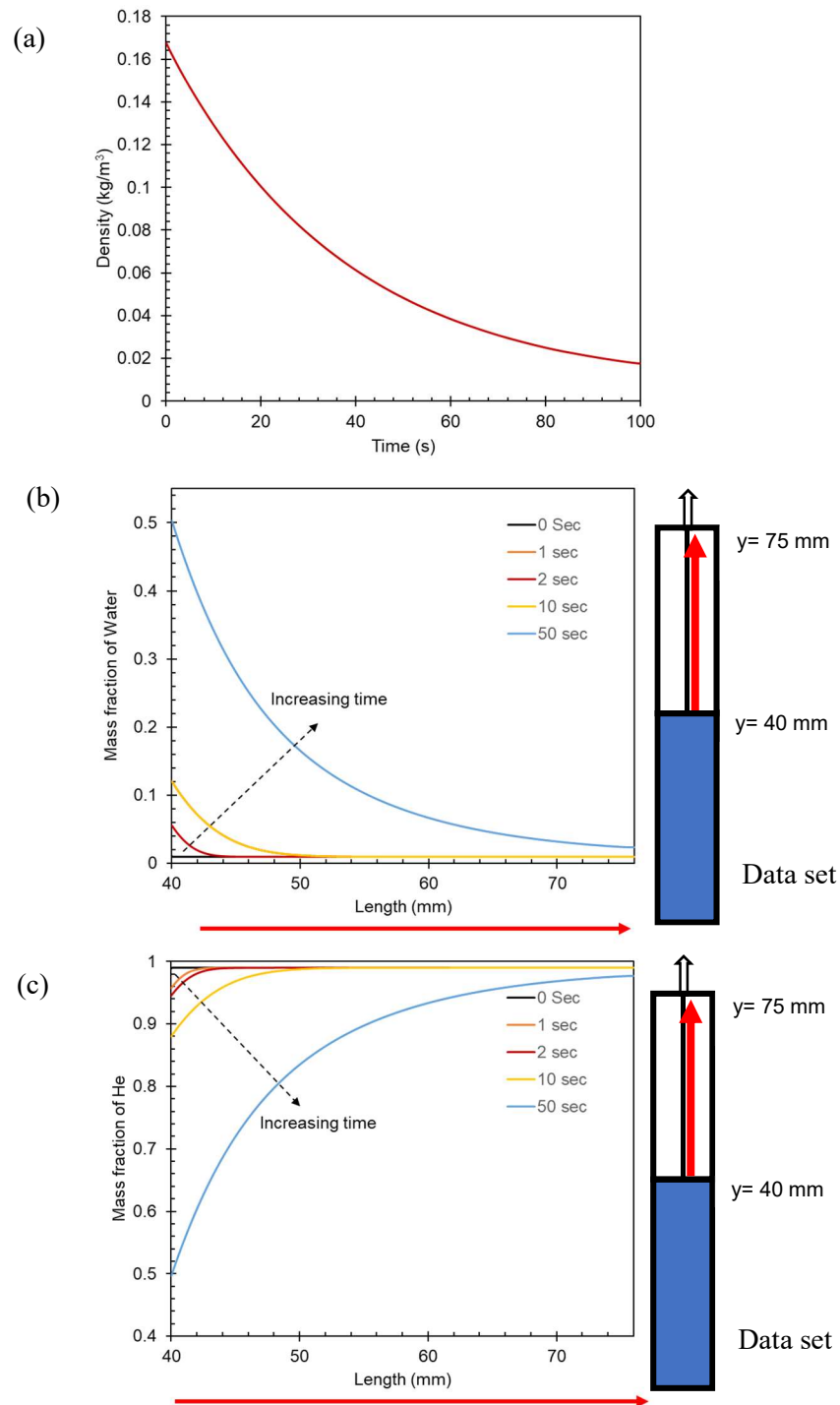


Figure 7.19: Change of density with time, and centerline distribution of mass fraction of (b) water vapor and (c) helium.

Since from Figure 7.19 we can conclude that reasonable results can be found by applying prescribed ‘mass flow rate’ outlet boundary condition instead of ‘pressure outlet’ boundary condition, therefore we have followed same approach to the full length scale computational domain (Figure 7.4) to validate our model by comparing the numerically obtained pressure with experimentally measured one. We have used the data taken from the experiment dated 05.11.2017. The experiment measures the outlet flow rate before and after desiccators. We have used flow rate measured before desiccators for the computational work.

Figure 7.20 shows the experimentally measured flow rate before the desiccator as a function of time which is a mixture of helium and water vapor. From the Figure 7.20, it can be observed that the vacuum process starts at ~ 350 s when outlet flow rate is at its maximum value of $0.0036 \text{ m}^3/\text{s}$. We focused on the first step in the vacuum process during when the maximum pressure reduction has taken place. This step spans from ~ 350 s to ~ 636 s. The flow rate starts to decrease exponentially from its initial value at 350s and reaches at a value of $\sim 0.0005 \text{ m}^3/\text{s}$ at the end of this step. Figure 7.21 shows the temporal variation of the pressure which follows the same trend as flow rate i.e., the maximum pressure reduction is occurring in between 350s. and 636s. As an initial attempt, we concentrate on simulating the first step of the vacuum process (350s to 636s.).

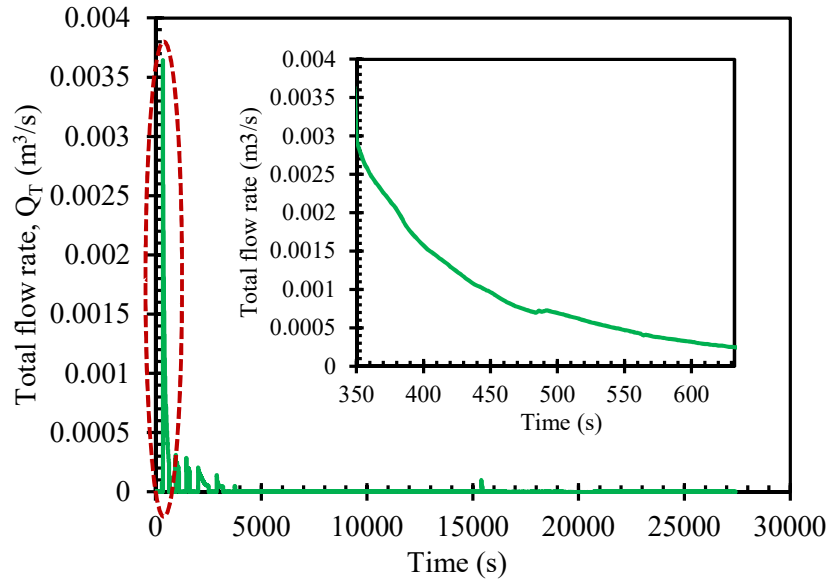


Figure 7.20: Temporal variation of flow rate.

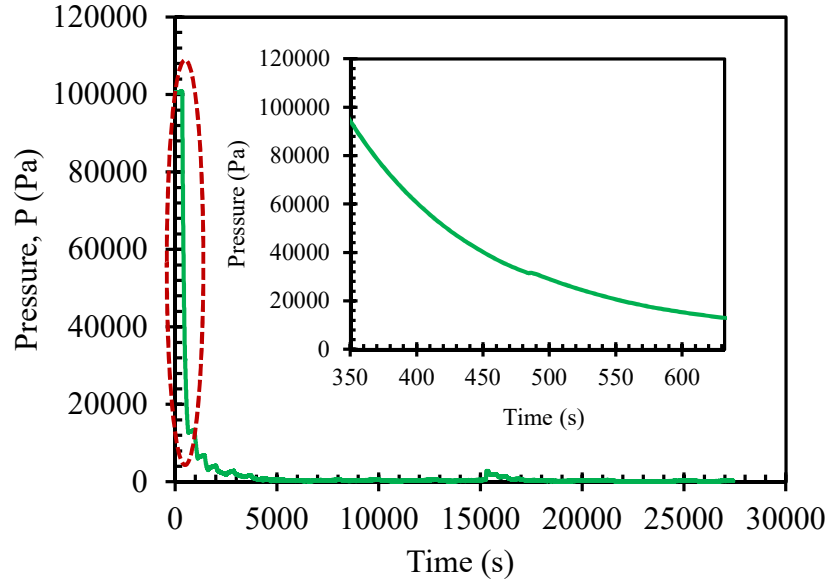


Figure 7.21: Temporal variation of pressure.

The experimental flow rate has been fitted with an exponential curve and prescribed at the outlet. The following time dependent flow rate, $Q(t)$ has been used in the simulation.

$$Q_T = 0.0024e^{-0.00} \quad (14)$$

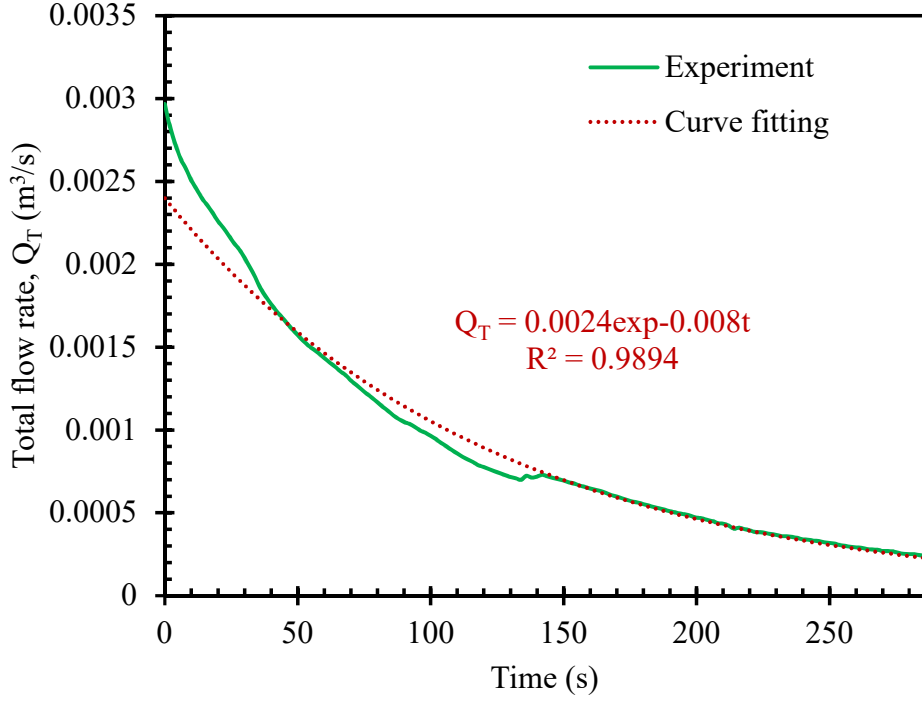


Figure 7.22: The temporal evolution of experimental flowrate fitted with an exponential function.

Since we are considering only the test rod as our computation domain, so we need to scale down the overall flow rate. Assuming, identical velocity magnitude, following scaling down approach has been taken.

$$v = \frac{Q_T}{A_T} = \frac{Q_s}{A_s} \quad (15)$$

$$Q_s = \frac{A_s}{A_T} Q_T = \frac{Q_T}{(A_T/A_s)} = \frac{Q_T}{SF} \quad (16)$$

Where, Q_T is the total flow rate, A_T is the internal cross-sectional area of the duct where flow rate is being measured, Q_s is the flow rate prescribed at the test rod outlet in the simulation study, A_s is the cross-sectional area of the test rod, SF is the scaling factor which is equal to 3.63 for our test condition. So, the modified flow rate for the test rod in computation becomes:

$$Q_s = \frac{Q_T}{SF} = \frac{1}{3.63} 0.0024e^{-0.008t} \quad (17)$$

To solve the energy conservation, we must prescribe a heat flux boundary condition on test rod surface. The total heat flux is a summation of conduction, convection, and radiation heat flux as shown in the following equation:

$$q'' = q''_{cond} + q''_{conv} + q''_{rad} \quad (18)$$

The empty space in the cask is filled with helium which is a poor conductor of heat. Besides, it is being pulled out of the system from the top. So, for simplicity, it can be assumed that heat is transmitted from the heater rod to the rest rod mainly by radiation. Therefore, for the time being, we are neglecting the convection and conduction heat transfer, considering the radiative flux as the main heat source which has been calculated by following Boltzmann radiation equation:

$$q'' = q''_{rad} = F\varepsilon\sigma(T_H^4 - T_s^4) \quad (19)$$

Where F is the shape factor, ε is the emissivity, σ is the Stefan constant $= 5.67 \times 10^{-8} W.m^{-2}.K^{-4}$, T_H and T_s is the is the experimentally measure heater rod and test rod temperature respectively.

To calculate the shape factor, we need to know the location of the heater rod and the test rod. Figure 7.23 shows the heater rod and test rod distribution. From the Figure 7.23, it can be seen that the test rod will mainly receive heat by radiation from heater rod 1 and 2. Therefore, for this report, we only considered heater rod 1 and 2 as the heat source. According to available literature, we assumed shape factor value as 0.1 [5-7]. Since the test rod is made by Zircaloy-4, hence we assumed emissivity of a constant value of 0.5 [8-9]. Figure 7.6 shows the variation of the heat flux with time.

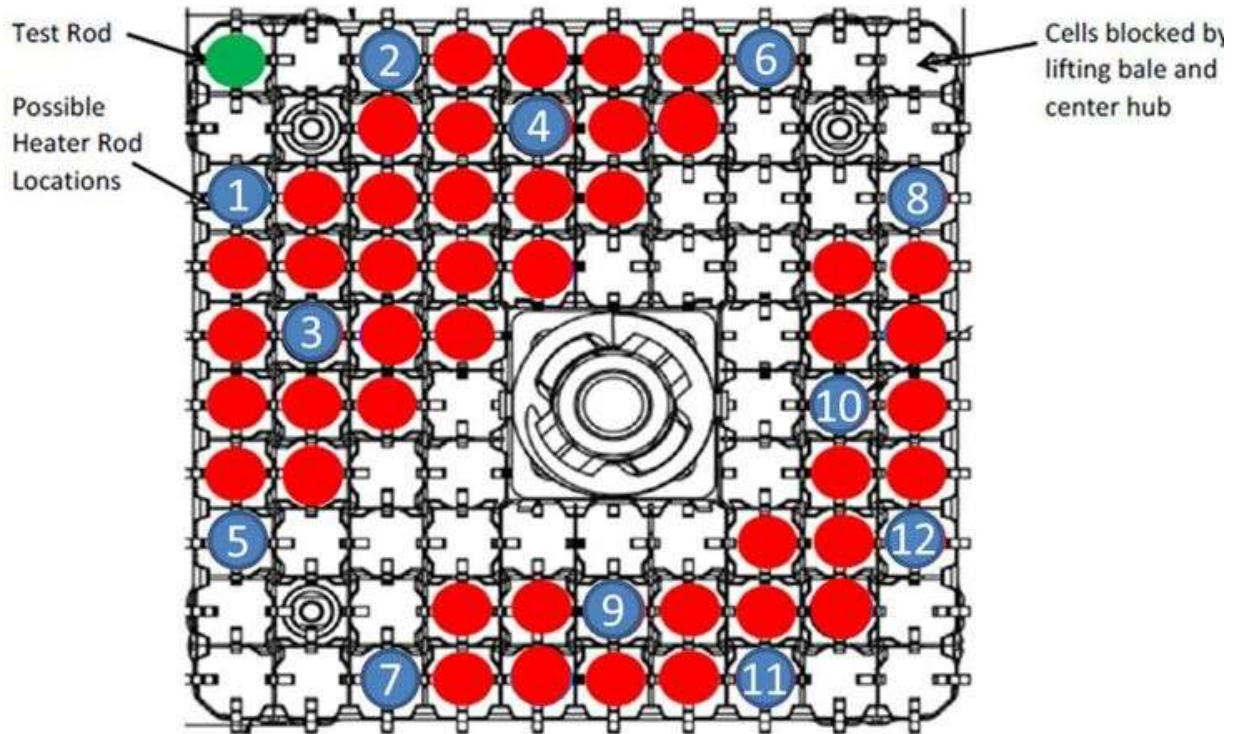


Figure 7.23: Test rod assembly

For this report, we applied a time averaged heat flux (31.31 w/m^2) corresponds to a total power of 3.94 W. After applying flow rate outlet boundary condition and also a constant heat flux on the two side walls of the computational test rod, we extracted the domain pressure and compared with the experimentally obtained pressure of the system as shown in Figure 7.25.

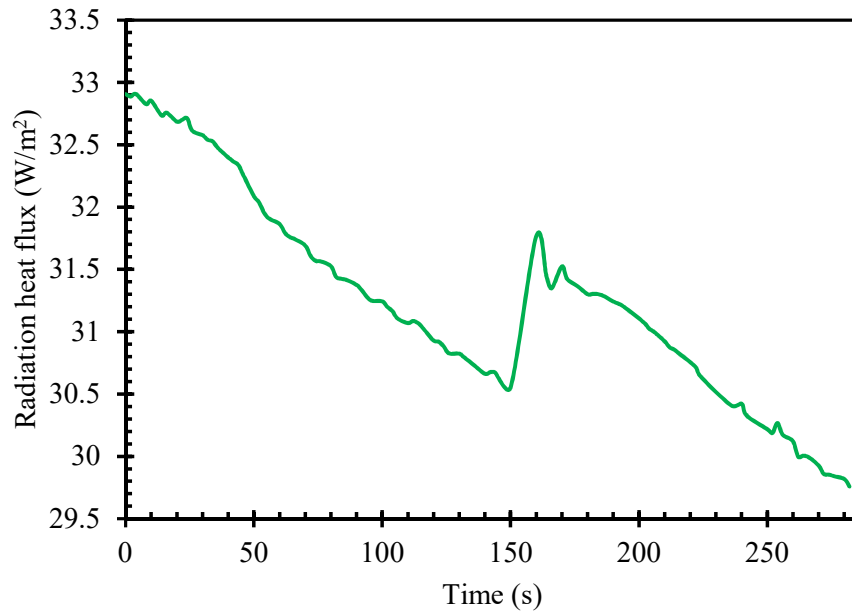


Figure 7.24: Temporal variation of the heat flux

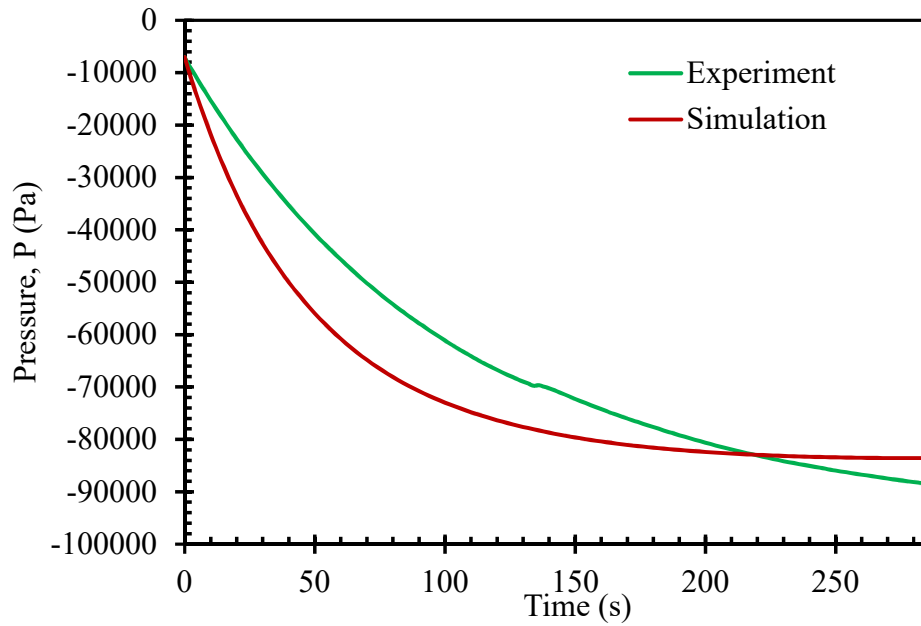


Figure 7.25: Comparison between the experimental and numerical pressure

Since we ignored the convection and conduction heat transfer mechanism, these assumptions initially lead to a significant deviation between experimental and numerical results

specially before 100 seconds as shown in Figure 7.25. On the contrary, this deviation reduces with time because in the vacuum condition, radiation is the most dominating heat transfer mechanism. From the Figure 7.25, it can also be seen that after ~200 seconds, the pressure shows a slightly increasing trend because of the significantly higher temperature. The immediate next plan of work is to apply a time varying heat flux instead of constant heat flux and also to address the conduction and convection effect on the overall heat flux.

Reference:

- [1] Knudsen, M., 1950, "The kinetic theory of gases."
- [2] Persad, A. H., and Ward, C. A., 2016, "Expressions for the evaporation and condensation coefficients in the Hertz-Knudsen relation," *Chemical Reviews*, 116(14), pp. 7727-7767.
- [3] Thomson, G. W., 1946, "The Antoine equation for vapor-pressure data," *Chemical Reviews*, 38(1), pp. 1-39.
- [4] Souli, M., and Zolesio, J. P., 2001, "Arbitrary Lagrangian–Eulerian and free surface methods in fluid mechanics," *Computer Methods in Applied Mechanics and Engineering*, 191(3–5), pp. 451-466.
- [5] S. B. Bopche and A. Sridharan, “Determination of view factors by contour integral technique,” *Ann. Nucl. Energy*, vol. 36, no. 11–12, pp. 1681–1688, 2009.
- [6] “Radiative view factors,” pp. 1–20.
- [7] L. Yang, W. Chen, L. Luo, and X. Zhao, “Calculation of radiation heat transfer view factors among fuel rod bundles based on CFD method,” *Ann. Nucl. Energy*, vol. 71, pp. 462–466, 2014.
- [8] J. Stuckert, M. Steinbrück , and U. Stegmaier, “On the thermo-physical properties of Zircaloy-4 and ZrO₂ at high temperatures Part 1 : Experimental and modeling results on cool-down of Zircaloy-4 rods in various atmospheres. Thermal and thermo-mechanical effects. A. Palagin, Part 2 : Determination of Zircaloy and ZrO₂ emissivities using experimental data of empty rods cool-down tests,” Nuclear Safety Institute, Russian Academy of Science, Moscow, January, 2002.
- [9] P. M. Mathew and I. M. George, “Total Emissivity of Zircaloy-4 at high temperatures,” *Proc. 17th Annu. CAN/CNS Conf*, 1996, vol. 1207, no. 8, pp. 2–5, 1996.